NIPER/BDM-0244

# TOPICAL REPORT

# APPLICATION OF WAVELET ANALYSIS TO UPSCALING OF ROCK PROPERTIES

**for**

**Management and Operating Contract for the Department of Energy's National Oil and Related Programs**

by

Lifu Chu and Richard Schatzinger

May 1996

Work Performed Under Contract No.
DE-AC22-94PC91008

Prepared for
U.S. Department of Energy
Bartlesville Project Office

**NIPER/BDM-0244**
**May 1996**

# APPLICATION OF WAVELET ANALYSIS TO UPSCALING OF ROCK PROPERTIES

**for**

**Management and Operating Contract for the Department of Energy's National Oil and Related Programs**

Work Performed Under Contract No.
DE-AC22-94PC91008

Prepared for
U.S. Department of Energy
Bartlesville Project Office

DISCLAIMER

This report was prepared as an account of work sponsored by an agency of the United States Government. Neither the United States Government nor any agency thereof, nor any of their employees, makes any warranty, expressed or implied, or assumes any legal liability or responsibility for the accuracy, completeness, or usefulness of any information, apparatus, product, or process disclosed, or represents that its use would not infringe privately owned rights. Reference herein to any specific commercial product, process, or service by trade name, trademark, manufacturer, or otherwise does not necessarily constitute or imply its endorsement, recommendation, or favoring by the United States Government or any agency thereof. The views and opinions of authors expressed herein do not necessarily state or reflect those of the United States Government or any agency thereof.

BDM-Oklahoma, Inc.
P.O. Box 2565

Bartlesville, Oklahoma 74005

# ABSTRACT

In this study, a new procedure was developed to significantly improve the computational efficiency and accuracy of upscaling for generating equivalent rock and rock-fluid properties under various geological and flow conditions based on multiresolution analysis of wavelet transforms. Additionally, a wavelet reconstruction method was explored to provide a basis for downsampling fine-scale rock property fields from information at various levels of coarser scale.

A number of tests were performed to verify the applicability of the newly developed upscaling procedure under realistic geological context. Test interbeds, interfacies, and geological structures were constructed by incorporating measurements from the Almond outcrop.

The test examples demonstrate that the new upscaling procedure generates excellent equivalent interbed rock properties under multiphase flow conditions. Simulation results also indicate that the wavelet transform method provides very reasonable upscaled interfacies rock and rock-fluid properties even for multiple lithologies and multiphase flow conditions.

# ACKNOWLEDGMENTS

This work was performed for the U.S. Department of Energy (DOE) under contract DE-AC22-94PC91008, Work Authorization NO. 95-A01, Revision B, task 1. The first author thanks Dr. Kraemer Luks, University of Tulsa subcontract manager, and other management personnel for their assistance and support. The authors also wish to thank the NIPER management and personnel who reviewed this manuscript and Dr. Robert Lemmon, DOE project manager, for his support.

# TABLE OF CONTENTS


**1.0 INTRODUCTION ..... 1**

**2.0 THEORETICAL BACKGROUND ..... 3**

2.1 Wavelet Transforms ..... 3

2.2 Multilevel Approximation with Wavelets ..... 5

2.3 Implementation of Discrete Wavelet Transform ..... 6

**3.0 DECOMPOSITION AND RECONSTRUCTION OF AN ABSOLUTE PERMEABILITY FIELD ..... 11**

3.1 One-Dimensional Case ..... 11

3.2 Two-Dimensional Applications ..... 14

**4.0 WAVELET ANALYSIS FOR TWO-PHASE FLOW ..... 17**

4.1 Upscaling Two-Dimensional Absolute Permeabilities ..... 18

4.2 Upscaling of Relative Permeabilities and Capillary Pressures ..... 19

4.2.1 Normalizing Saturation ..... 19

4.2.2 Determining Saturation Distributions ..... 20

4.2.3 Upscaling Saturation ..... 20

4.2.4 Upscaling Capillary Pressures and Phase Permeabilities ..... 20

4.2.5 Weighting the Capillary Pressures and Phase Permeabilities ..... 20

4.2.6 Upscale Relative Permeabilities ..... 21

4.3 Application Examples ..... 21

4.3.1 Geological Constraint on Outcrop Permeability Mapping ..... 22

4.3.2 Rock-Fluid Properties ..... 32

4.3.3 Interbedset Upscaling ..... 32

4.3.4 Interfacies Upscaling ..... 36

**5.0 CONCLUSIONS ..... 41**

**6.0 NOMENCLATURE ..... 43**

**7.0 REFERENCES ..... 45**

# TABLES

4–1 Comparison of Permeability between Major Bedsets within Tidal Channel 1 ..... 26
4–2 Comparison of Permeability between Major Bedsets within Tidal Channel 2 ..... 26
4–3 Average Petrophysical Properties for Horizontally Oriented Plugs ..... 27
4–4 Statistical Parameters of Facies ..... 29
4–5 Parameters for Relative Permeabilities ..... 32
4–6 Parameters for Capillary Pressures ..... 32

# FIGURES

2–1 One-Dimensional Recursive Decomposition and Reconstruction ..... 8
2–2 A 2D Recursive Decomposition and Reconstruction ..... 10
3–1 Decomposition of 1D Permeabilities ..... 12
3–2 Detailed Signals at Each Step of Reconstruction ..... 13
3–3 Comparison of the Original and Reconstructed Permeability Distributions ..... 14
3–4 Original Permeability Distribution for Three Lithologies Case ..... 15
3–5 Upscaled Permeability Distribution at Level 1 for Three Lithologies Case ..... 15
3–6 Upscaled Permeability Distribution at Level 2 for Three Lithologies Case ..... 16
3–7 Reconstructed Permeability Distribution for Three Lithologies Case ..... 16
4–1 Almond Formation Outcrop G Tidal-Channel 1 Bedset Boundaries. Datum is base of outcrop ..... 22
4–2 Distribution of Major Bedsets of the Tidal-Delta Facies at Almond Formation Outcrop G Based on a Photomosaic. Marked horizontal distances are feet north of the southern margin of the outcrop. Horizontal scale is not constant due to unequal distance of individual photographs comprising the photomosaic. Vertical scale varies somewhat along the profile for the same reason. Note the overall northward sense of offset of successively younger bedsets. ..... 23
4–3 This Figure Is a Reconstruction of the Geologically Constrained Distribution of Permeability within the Bottom 5 ft of the Tidal Delta Whose Major Bedsets Are Outlined in Figure 4–2. Note the northward dip and rapid changes of permeability in the vertical direction.

Extreme vertical exaggeration causes the major bedset boundaries
to assume a sinusoidal geometry. ..... 24

4–4 Closely Spaced Core Plug Samples from a 1-ft-Thick Northward Dipping, Planar Cross-Bedded Tidal Swash Bar within the Foreshore Facies Illustrate the Fine Detail of Permeability Variations within the Bedset and That Is Parallel to the Bedding Direction. Individual Sandstone Laminae are Less than 1 cm Thick. ..... 25

4–5 Semivariogram of Permeability for the Tidal-Channel Facies ..... 28

4–6 Semivariogram of Permeability for Tidal-Delta Facies ..... 28

4–7 Semivariogram of Permeability for Beach Facies ..... 29

4–8 A Realization of Permeability Distribution within the Tidal-Channel Facies Based on Outcrop Samples ..... 30

4–9 A Realization of Permeability Distribution within the Beach Facies Based on Outcrop Samples ..... 31

4–10 A Realization of Permeability Distribution within the Tidal-Delta Facies Based on Outcrop Samples ..... 31

4–11 Comparison of Production Performances from Original and Upscaling Systems (Beach Facies) ..... 33

4–12 Comparison of Water Cut at Production Wells from Original and Upscaling Systems (Beach Facies) ..... 34

4–13 Comparison of Production Performances from Original and Upscaling Systems (Tidal-Delta Facies) ..... 34

4–14 Comparison of Water Cut at Production Wells from Original and Upscaling Systems (Tidal-Delta Facies) ..... 35

4–15 Comparison of Production Performances from Original and Upscaling Systems (Tidal-Channel Facies) ..... 35

4–16 Comparison of Water Cut at Production Wells from Original and Upscaling Systems (Tidal-Channel Facies) ..... 36

4–17 A Realization of Permeability Distribution within the Tidal-Delta and Beach Facies Based on Outcrop Samples ..... 37

4–18 A Realization of Permeability Distribution within the Tidal-Channel and Beach Facies Based on Outcrop Samples ..... 37

4–19 Comparison of Production Performances from Original and Upscaling Systems (Tidal-Channel and Beach Composite System) ..... 38

4–20 Comparison of Water Cut at Production Wells from Original and Upscaling Systems (Tidal-Channel and Beach Composite System) ..... 39

4–21 Comparison of Production Performances from Original and Upscaling Systems (Tidal-Delta and Beach Composite System) ..... 40

4–22 Comparison of Water Cut at Production Wells from Original and Upscaling Systems (Tidal-Delta and Beach Composite System) ..... 40

# EXECUTIVE SUMMARY

Although numerous upscaling techniques are reported in the literature, efficiently computing reasonably accurate equivalent rock properties from geological data at fine scale remains difficult. This is especially true for facies with multiple lithologies under multiphase flow conditions. Due to the nature of multiscale heterogeneity inherent to petroleum reservoirs, the equivalent rock and flow properties will vary with the scales of heterogeneity. Therefore, upscaled properties under multiphase flow conditions cannot be estimated without reference to the absolute scales of heterogeneity.

Wavelet analysis is a multiresolution framework and, thus, it is well suited for upscaling rock and flow properties in a multiscale heterogeneous reservoir. The compact support property of the wavelet transform assures efficient computation. Choices of regularity provides a flexible way to control the smoothness of the resulting upscaling properties.

In this study, we developed a new procedure to upscale rock and rock-fluid properties under single- and multi-phase flow conditions using wavelet transform. The beauty of the method is that since the equivalent properties at different length scales are computed recursively, the interdependent influences of the heterogeneities on the scales are included effectively. The method is demonstrated by successfully applying it to upscale interbedset and interfacies outcrop petrophysical data.

By using the newly developed procedure to upscale the measurements from Almond Formation outcrops, we demonstrated that the wavelet transform generates excellent equivalent property distributions under multiphase flow within a single geological facies. Simulation results also indicated that the wavelet transform method provides very reasonable upscaling results even when multiple lithologies are considered under multiphase flow conditions. Because the upscaled property images obtained from wavelet transform capture the characters of the original property fields, the predicted performance from upscaling property fields matches well with the one from the original fine-scale property fields.

# 1.0 INTRODUCTION

Wavelets constitute unconditional bases for a variety of function spaces. Thus, they can provide accurate approximations of functions in such space. An approximate representation of a function (or a process) using wavelets is provided by an infinite series expansion of dilated and translated versions of a base wavelet. For functions with finite energy this wavelet representation is optimal, i.e., it offers the closest approximation to the original function, in the least square sense.

The wavelet transform has become pervasive in diverse areas such as mathematics, physics, computerized visualization, digital signal processing (Mallat 1989a, b), numerical analysis (Bacry et al. 1993), and geophysics (Davis et al. 1994) since it was formalized by several researchers (Morlet et al. 1982a, b; Grossmann and Morlet 1984) in early 1980's, and later by Meyer (1993a, b), Mallat (1989a, b), and Daubechies (1988, 1992). Very recently, wavelet analysis also has been used in petroleum engineering to enhance rock property images, denoise the measurements of rock properties (Panda 1994), and solve flow equations (Moridis et al. 1995) and in environmental engineering to downsample the absolute permeability (Brewer and S. Wheatcraft 1994).

Upscaling reservoir properties is a complicated and challenging problem, and remains an unsolved problem, especially for multiple lithologies and multiphase flow conditions. Although upscaling problems are traditionally considered a process to upsample the rock properties or/and rock-fluid properties to appropriate, coarser grids using fine grid information, the more realistic or practical requirements for upscaling should be upsampling the properties for coarser grids using all available information at all levels of finer grids. With multiresolution analysis properties, compact support, orthogonality, and localized transforms in both space and frequency domains, wavelet analysis becomes an ideal candidate for such purposes.

In this study, we developed a decomposition and reconstruction procedure for rock property fields in light of Mallat's work (1989a). Application of the developed procedure to absolute permeability fields presents promising results. When coarsening fine grid permeability to more accessible scales, although the number of grids are reduced substantially, the main trends or characters of the permeability fields are reasonably well preserved. The flow behavior from the original fine grid permeability field is reproduced perfectly by the upscaled permeability field. The developed method can also adequately reconstruct the fine-scale properties from coarser scale information.

Encouraged by the above successful application of the wavelet transform, we further extend the method to upscale not only rock properties but also rock-fluid properties for multiple lithologies and multiphase flow conditions.

To verify the applicability of the newly developed upscaling procedure within a realistic geological context, we constructed testing problems using measurements from the Almond Formation.

# 2.0 THEORETICAL BACKGROUND

## 2.1 Wavelet Transforms

Wavelet transforms, like the extensively used Fourier transform, are also kinds of linear integral transforms. To understand the mechanism of the wavelet transforms, one may begin discussion with the familiar Fourier transform. Recall that for a given function, $f(x)$, the corresponding Fourier transform takes the form,

$$\hat{f}(\omega) = \int_{-\infty}^{\infty} f(u) e^{-i\omega u} du \tag{2–1}$$

Although the above transform gives information about the content of a function in frequency domain, it gives no information about the location of these frequencies in the spatial domain. Therefore, strictly speaking, Fourier transform is applicable to a "homogeneous" system, or otherwise only extracts "blend" properties.

Spatially varying phenomena are quite common in the real world, such as in seismic signal, non-stationary geophysical processes, or in reservoir rock property distributions. To extract information from such processes, Fourier transform alone is, therefore, quite inadequate. This is because although Fourier transform gives the information of certain frequencies, this information cannot be effectively used as it is not spatially localized. Ideally, one would like to have space and frequency information simultaneously. One of the methods which gives the space-frequency representation of a function (or process) but still remains within the Fourier transform framework is windowed Fourier transform. By windowed Fourier transform, spatial localization can be obtained by convoluting a windowing function $g(x)$ with the conventional Fourier transform as follows:

$$Gf(\omega,x) = \int_{-\infty}^{\infty} f(u) g(u-x) e^{-i\omega u} du \int_{-\infty}^{\infty} f(u) g_{\omega,x} e^{-i\omega u} du \tag{2–2}$$

where $\omega$ is the frequency, $x$ is the location of the center of the window. $Gf(\omega,x)$ describes the spectral content of $f(x)$ around $x$ within the window defined by $g(x)$.

Despite an ability to spatially localize information, the windowed Fourier transform suffers from several limitations. For example, because the spatial localization precision of the windowed Fourier transform is controlled by standard deviation of $g_{w,x}$, $\sigma_g$, if there are important local transient components of differing support size, then one cannot find a universally optimal $g(x)$ for effectively and precisely analyzing the process. The wavelet

transform was developed to address such limitations of windowed Fourier transform and other similar transforms.

The wavelet transform is defined as a convolution of a given function, $f(x)$, with a kernel function, $\psi_{\lambda,x}(u) = \frac{1}{\sqrt{\lambda}}\psi(\frac{u-x}{\lambda})$, and is given as

$$Wf(\lambda,x) = \int_{-\infty}^{\infty} f(x)\psi_{\lambda,x}(u)du = \int_{-\infty}^{\infty} f(x)\frac{1}{\sqrt{\lambda}}\psi(\frac{u-x}{\lambda})du \qquad \lambda > 0 \tag{2–3}$$

Here $\lambda$ is a scale parameter, $x$, is a location parameter, and a family of functions, $\psi_{\lambda,x}(u)$, are called wavelet functions.

In contrast to the constant support length of the windowing function, $g(x)$, in the windowed Fourier transform the support length of wavelet functions, $\psi_{\lambda,x}(u)$, changes proportionally with the scale parameter, $\lambda$, i.e., increasing $\lambda$ will dilate and decreasing $\lambda$ will contract the wavelet function. In this way, in small scale, the wavelet function will have small support length, therefore wavelet transform will pick up higher frequency components and vice-versa. Just as in the Fourier transform, one can also develop discrete version of the above continuous wavelet transforms for analyzing discrete data sequences.

Ideally, one would prefer both the support length and moving incremental step of the wavelet function to be small in small scale and vice-versa. This can be easily accomplished by relating them to level of scale, $m$, or explicitly define:

$$\lambda = \lambda_0^m \tag{2–4}$$

and

$$x = nx_0\lambda_0^m \tag{2–5}$$

where $\lambda_0$ is a fixed dilation step greater than 1, $x_0$ is initial step at scale $0$, and $n$ is an integer, representing spatial index of data sequence. For the convenience of computation, one may assign, $\lambda_0 = 2$ and normalize the initial system so that $x_0 = 1$. With the above convention, a family of wavelet functions can be rewritten as

$$\psi_{m,n}(x) = \frac{1}{\sqrt{2^m}}\psi(2^{-m}x - n) \tag{2–6}$$

Accordingly, the discrete wavelet transform takes the form:

$$\langle f, \psi_{m,n} \rangle = \int f(u)\psi_{m,n}(u)du \tag{2–7}$$

## 2.2 Multilevel Approximation with Wavelets

It was proven (Mallat 1989a) that if subspace $(V_m)_{m \in z}$ is a multiresolution approximation of $L^2(R)$, then there exists a unique wavelet function, $\psi(x) \in L^2(R)$, such that

$$2^{-m}\psi(2^{-m}x - n) \tag{2–8}$$

is a complete orthonormal basis of $V_m$, i.e.,

$$\int \psi_{m,n}(x)\psi_{m',n'}(x)dx = \delta_{m,m'}\delta_{n,n'} \tag{2–9}$$

where $\delta_{i,j}$ is the Kronecker delta function.

This implies that all the functions with finite energy can be approximated, up to arbitrary high precision, by a linear combination of the wavelet functions, $\psi_{m,n}(x)$, i.e.,

$$f(x) = \sum_{m=-\infty}^{\infty} \sum_{n=-\infty}^{\infty} D_{m,n}\psi_{m,n}(x). \tag{2–10}$$

Similar to Fourier series, the coefficients, $D_{m,n}$, are obtained by wavelet transform of $f(x)$,

$$D_{m,n} = \langle f, \psi_{m,n} \rangle = \int f(u)\psi_{m,n}(u)du \tag{2–11}$$

If one lets $\phi_{m,n}(x)$, a scaling function, be the basis of another subspace, $(W_m)_{m \in z}$, which is the orthogonal complement of $(V_m)_{m \in z}$, then it is further proven that

$$f(x) = \sum_{m=-\infty}^{\infty} \langle f, \phi_{m^*,n} \rangle \phi_{m^*,n}(x) + \sum_{m=-\infty}^{m^*} \sum_{n=-\infty}^{\infty} \langle f, \psi_{m,n} \rangle \psi_{m,n}(x) \tag{2–12}$$

where $m^*$ is an intermediate scale.

After a few steps of algebraic manipulation, one can obtain a recursive, multiresolution representation of the function, $f(x)$ as:

$$P_{m-1} f(x) = P_m f(x) + Q_m f(x) \tag{2–13}$$

where

$$Q_m f(x) = \sum_{n=-\infty}^{\infty} \langle f, \psi_{m,n} \rangle \psi_{m,n}(x) = \sum_n E_{m,n} \psi_{m,n}(x) \tag{2–14}$$

and

$$P_m f(x) = \sum_{n=-\infty}^{\infty} \langle f, \phi_{m,n} \rangle \phi_{m,n}(x) = \sum_n D_{m,n} \phi_{m,n}(x) \tag{2–15}$$

are orthogonal projections of $f(x)$ onto subspaces $W_m$ and $V_m$, respectively. Coefficients $D_{m,n}$ and $E_{m,n}$ are conventionally called discrete approximation and discrete detail signals of $f(x)$ at scale $m$ and location $n$.

Equation (2–13) indicates that the discrete approximation at a finer scale $m-1$ can be reconstructed from discrete approximation and detail signal at a coarser scale, $m$.

## 2.3 Implementation of Discrete Wavelet Transform

For a given data sequence $\{c_n\}$ corresponding to a function $f(x)$ and a chosen $\phi(x)$, one can assume this data sequence is equal to the discrete approximation of $f(x)$ at finest scale level $m = 0$, i.e.,

$$\{D_{0,n}\} = \{\langle f, \phi_{0,n} \rangle\} = \{c_n\}. \tag{2–16}$$

Referring to Equation (1–15), using one construct in $V_0$

$$P_0 f(x) = \sum_n D_{0,n} \phi_{0,n}(x). \tag{2–17}$$

from Equation (2–13), one can decompose $P_0 f(x)$ into its orthonormal components along subspaces, $V_1$ and $W_1$, respectively, i.e.,

$$\begin{aligned} P_0 f(x) &= \sum_n D_{0,n} \phi_{0,n} = P_1 f(x) + Q_1 f(x) \\ &= \sum_k D_{1,k} \phi_{1,k} + \sum_k E_{1,k} \psi_{1,k} \end{aligned} \tag{2–18}$$

the sequences, $\{D_{1,k}\}$ and $\{E_{1,k}\}$, can be determined as a function of $\{D_{0,n}\}$ using wavelet transform,

$$D_{1,k} = \langle \phi_{1,k}, P_0 f \rangle = \sum_n D_{0,n} \langle \phi_{1,k}, \phi_{0,n} \rangle \tag{2–19}$$

and

$$E_{1,k} = \langle \psi_{1,k}, P_0 f \rangle = \sum_n D_{0,n} \langle \psi_{1,k}, \phi_{0,n} \rangle \tag{2–20}$$

where

$$\langle \phi_{1,k}, \phi_{0,n} \rangle = 2^{-1/2} \int \phi(x/2)\phi(x-(n-2k))dx \tag{2–21}$$

and

$$\langle \psi_{1,k}, \phi_{0,n} \rangle = 2^{-1/2} \int \psi(x/2)\phi(x-(n-2k))dx \tag{2–22}$$

if one defines

$$h(n) = 2^{-1/2} \int \phi(x/2)\phi(x-n)dx \tag{2–23}$$

and

$$g(n) = 2^{-1/2} \int \psi(x/2)\phi(x-n)dx \tag{2–24}$$

respectively, one can simplify Equations (2–19) and (2–20) as

$$D_{1,k} = \sum_n h(n-2k) D_{0,n} \tag{2–25}$$

and

$$E_{1,k} = \sum_n g(n-2k) D_{0,n} \tag{2–26}$$

or in matrix form

$$D^1 = HD^0 \tag{2–27}$$

and

$$E^1 = GD^0 . \tag{2–28}$$

It is easy to prove that one can recursively determine sequences $D^m$ and $E^m$ from $D^{m-1}$ by

$$D^m = HD^{m-1} \tag{2–29}$$

and

$$E^m = GE^{m-1}. \tag{2–30}$$

The above procedure is usually called decomposition, and H and G are called low pass filter and high pass filter, respectively. The reconstruction procedure can be computed as easily as decomposition. Since

$$P_{m-1} f(x) = \sum_n D_{m-1,n}\phi_{m,n} = P_m f(x) + Q_m f(x)$$

$$= \sum_k D_{m,k}\phi_{m,k} + \sum_k E_{m,k}\psi_{m,k} \tag{2–31}$$

hence

$$D_{m-1,n} = \langle \phi_{m-1,n}, P_{m-1} f \rangle = \sum_k D_{m,k}\langle \phi_{m-1,n}, \phi_{m,k} \rangle + \sum_k E_{m,k}\langle \phi_{m-1,n}, \psi_{m,k} \rangle)$$

$$= \sum_k h(n-2k)D_{m,k} + \sum_k g(n-2k)E_{m,k}, \tag{2–32}$$

or in matrix form as

$$D^{m-1} = H^T D^m + G^T E^m. \tag{2–33}$$

Overall, decomposition of a data sequence $c_0$ into the mutually orthonormal subspaces $V$ and W using wavelet transforms can be pictorially represented as in Figure 2–1a, and the corresponding reconstruction procedure can be shown as in Figure 2–1b.

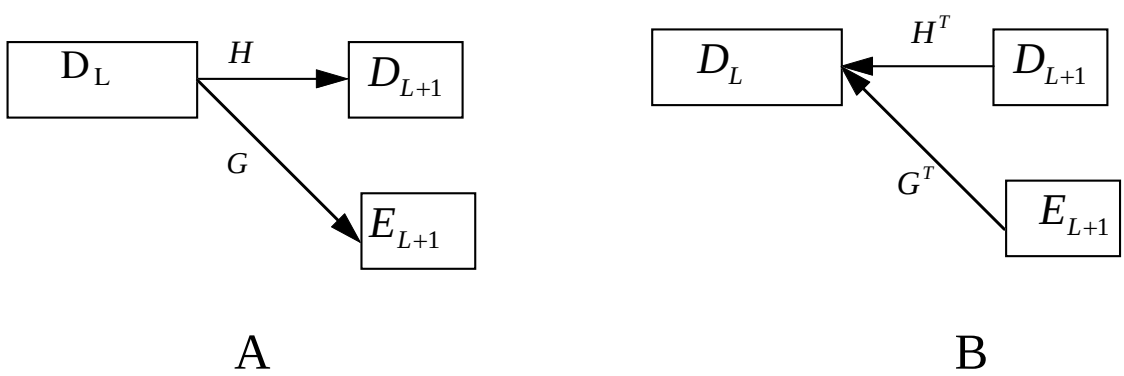

**Figure 2–1 One-Dimensional Recursive Decomposition and Reconstruction**

The above procedures for one-dimensional (1D) data sequence can be extended to two-dimensional (2D) multiresolution approximation using the separable assumption which states that each vector space $V_m$ can be decomposed as a tensor product of two identical subspaces $V_m^{'}$ of $L^2(R)$. Based on this assumption, the scaling function for the 2D case is related to corresponding 1D scaling function by

$$\phi(x_1, x_2) = \phi(x_1)\phi(x_1) \tag{2–34}$$

There are a total of four orthonormal basis for the 2D case. According to Mallat (1989a), the other three can be constructed using corresponding wavelet function and scaling function for 1D case as follows:

$$\psi^1(x_1, x_2) = \phi(x_1)\psi(x_2), \tag{2–35a}$$

$$\psi^2(x_1, x_2) = \psi(x_1)\phi(x_2), \tag{2–35b}$$

and

$$\psi^3(x_1, x_2) = \psi(x_1)\psi(x_2). \tag{2–36}$$

where $\psi(x)$ is the 1D wavelet function associated with scaling function, $\phi(x)$.

Similar to 1D case, the projection of the function, $f(x_1, x_2)$, on scaling subspace $V$ is obtained by

$$P_m f(x_1, x_2) = \langle f, \phi_{m,nk} \rangle = \langle f, \phi_{m,n}\phi_{m,k} \rangle \tag{2–37}$$

and projections of $f(x_1, x_2)$ on wavelet subspace are given by

$$Q_m^1 f(x_1, x_2) = \langle f, \psi_{m,nk}^1 \rangle = \langle f, \phi_{m,n}\psi_{m,k} \rangle, \tag{2–38}$$

$$Q_m^2 f(x_1, x_2) = \langle f, \psi_{m,nk}^2 \rangle = \langle f, \psi_{m,n}\phi_{m,k} \rangle, \tag{2–39}$$

and

$$Q_m^3 f(x_1, x_2) = \langle f, \psi_{m,nk}^3 \rangle = \langle f, \psi_{m,n}\psi_{m,k} \rangle. \tag{2–40}$$

The corresponding discrete approximation can be written as

$$D_m = HD_{m-1}H^T \tag{2–41}$$

and the three detail signals can be given by

$$E_m^1 = HD_{m-1}G^T, \tag{2–42}$$

$$E_m^2 = GD_{m-1}H^T, \tag{2–43}$$

and

$$E_m^3 = GD_{m-1}G^T. \tag{2–44}$$

Similar to the 1D case, the reconstruction algorithm can be computed by

$$D_{m-1} = H^T D_m H + G^T D_m H + G^T E_m G + H^T D_m G \tag{2–45}$$

The algorithm for multiresolution analysis using wavelet for 2D data sequence is schematically shown in Figures 2–2a and 2–2b for decomposition and reconstruction, respectively.

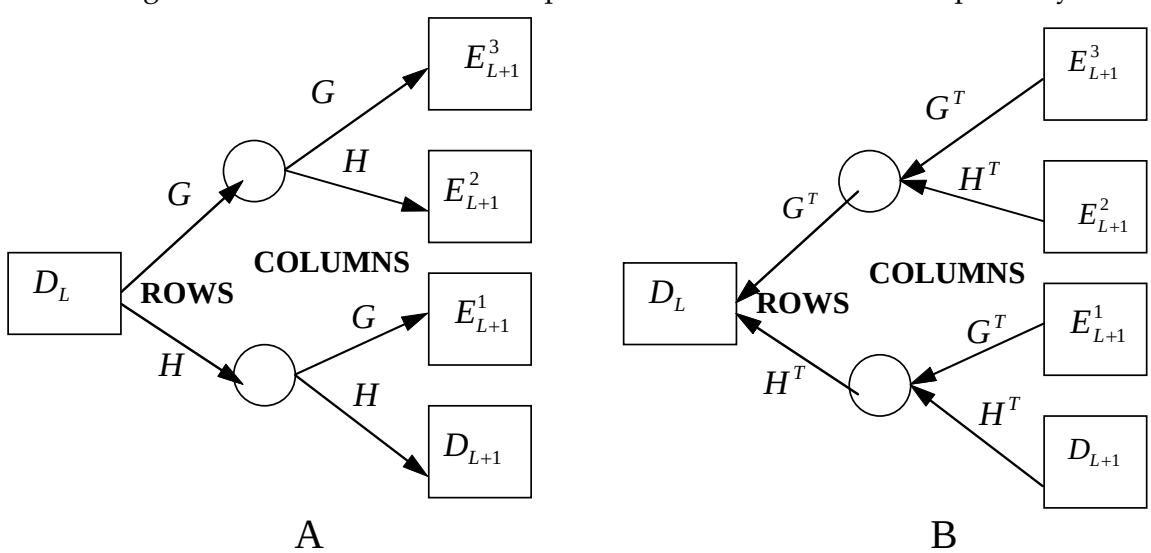


**Figure 2–2 A 2D Recursive Decomposition and Reconstruction**

# 3.0 DECOMPOSITION AND RECONSTRUCTION OF AN ABSOLUTE PERMEABILITY FIELD

It is well known that petroleum reservoirs are inherently heterogeneous and that flow performance of reservoirs is controlled by variability in reservoir properties at various scales. The dominant scale effects will vary with the production processes involved. Therefore, to accurately describe reservoir performance, one needs to develop a method to first adequately reconstruct the fine-scale variability from sparsely distributed, coarser, multiscale samples, and then properly coarsen the fine-scale variability whenever necessary. Here, the procedure presented in the previous sections is used to upscale and downscale the absolute permeability distributions. Reconstruction algorithm begins with the determination of the detail signals at all levels of scale. Essentially, such information is not available since full spatial coverage of discrete approximation at all scales will rarely occur for practical application. Therefore, one usually needs to assign stochastic values for all detailed signals based on a pseudo-fractal relationship (Wornell and Oppenheim 1992). Since reconstruction is not our current concern, assume that all the detail signals are known. The main issue here is to examine how the permeability variability transforms in both directions between the scales. To demonstrate the applicability of the procedures, two examples are presented: a 1D permeability distribution and a 2D case.

## 3.1 One-Dimensional Case

The original permeability distribution is shown in Figure 3–1a. Notice that there is a peak in permeability around $x = 73$. After three steps of decomposition following the procedure depicted in Figure 2–1a, we obtained the upscaling permeability distributions at each coarser scale, which is shown in Figures 3–1b, 3–1c, and 3–1d, respectively. Notice that although the decomposition process tends to blend the property details, and the permeability distribution gradually becomes smoother and smoother, the permeability peak still exists even at scale level 3. Furthermore, when decomposing the permeability field, the higher frequency components will gradually disappear, but such information is never lost. The permeability differences between the different scales are kept as detail signals. Figure 3–2 shows the detail signals at different levels of scale. It is known that the equivalent value for a 1D permeability in a series arrangement is equal to the harmonic average of the permeabilities. Because the harmonic average of the permeability at each coarser scale is 1013.7 md, 1023.1 md, 1028.6 md, and 1066.3 md, which are all very close to the harmonic average of the original permeability field, 1012 md, one should expect that the flow behavior for the upscaling system will match the behavior of the original system. The small deviations in the harmonic average may be from the imposed periodic boundary conditions.

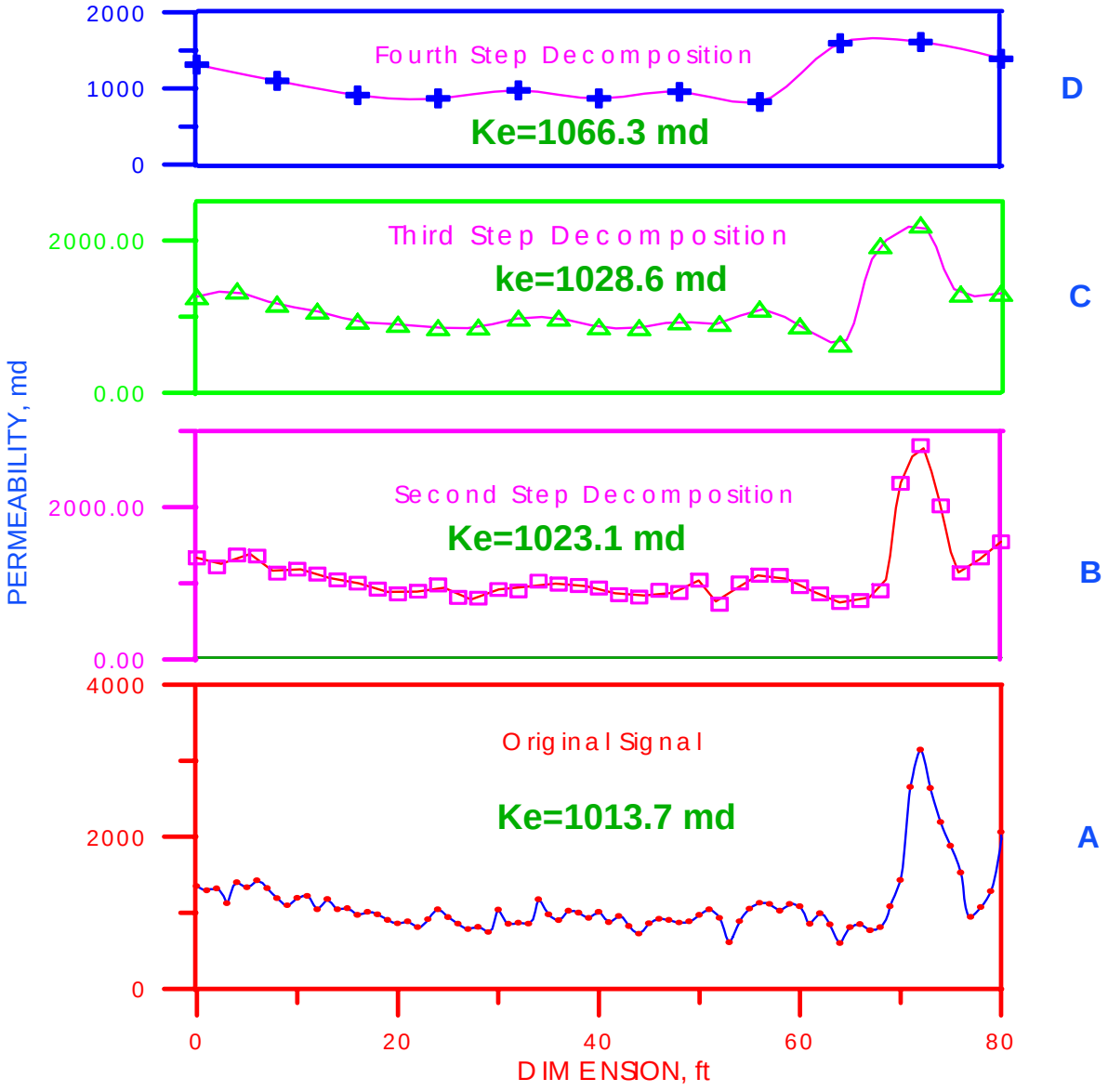


**Figure 3-1 Decomposition of 1D Permeabilities**

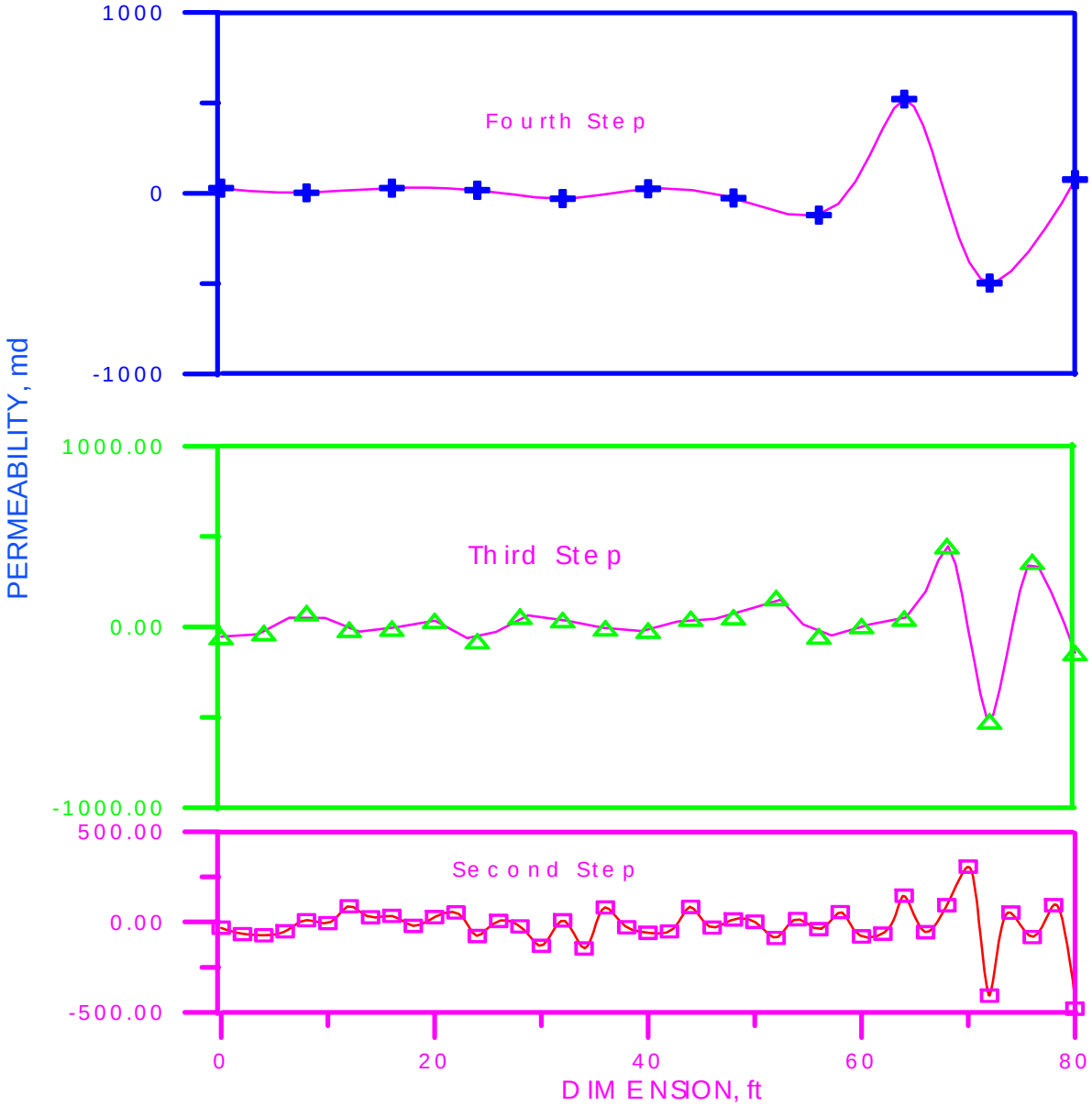


**Figure 3–2 Detailed Signals at Each Step of Reconstruction**

To examine the reconstruction procedure, reconstruct the permeability distribution at original scale using discrete approximation at final step shown in Figure 3–1d and the detail signals shown in Figure 3–2. The comparison between the original and the reconstructed permeability distribution is shown in Figure 3–3. Notice that the match between the two distributions is almost exact.

## 3.2 Two-Dimensional Applications

This section presents the results of decomposing and reconstructing a 2D permeability field following the procedure shown in Figure 2–2. The original permeability field shown in Figure 3–4 is composed of three lithologies with the means for each lithology being 100 md, 10 md, and 1 md, respectively. The upscaling permeability distributions at different scales generated from the proposed procedure are shown in Figures 3–5 and 3–6. Analogous to the 1D case, after decomposition, the details of the permeability distribution gradually disappeared; however, the main characters of the original distribution are well captured. Using discrete approximation and three detail signals (not shown here) at each scale, the permeability distribution at original scale is reconstructed, as shown in Figure 3–7. Except for slight differences along the boundaries, the reconstructed permeability image matches the original one very well (Figure 3–4).

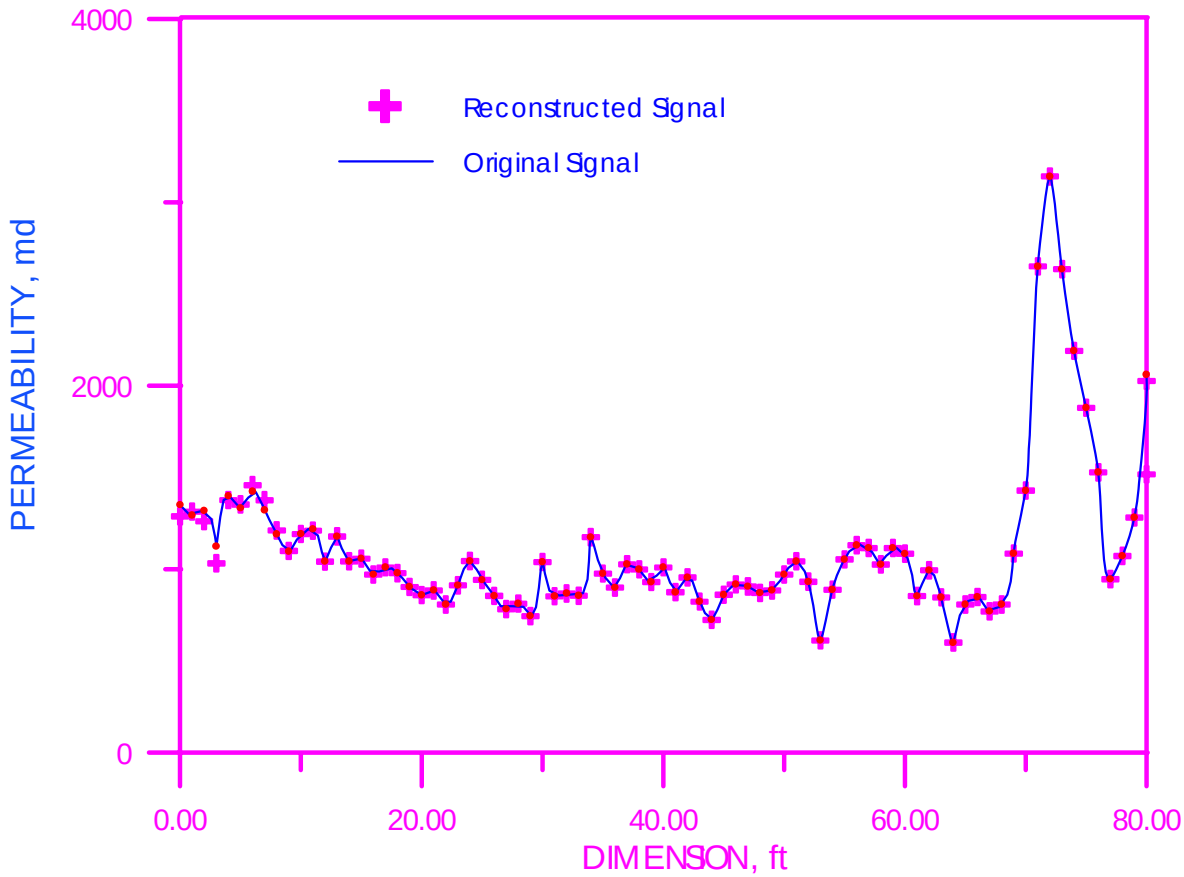


**Figure 3–3 Comparison of the Original and Reconstructed Permeability Distributions**

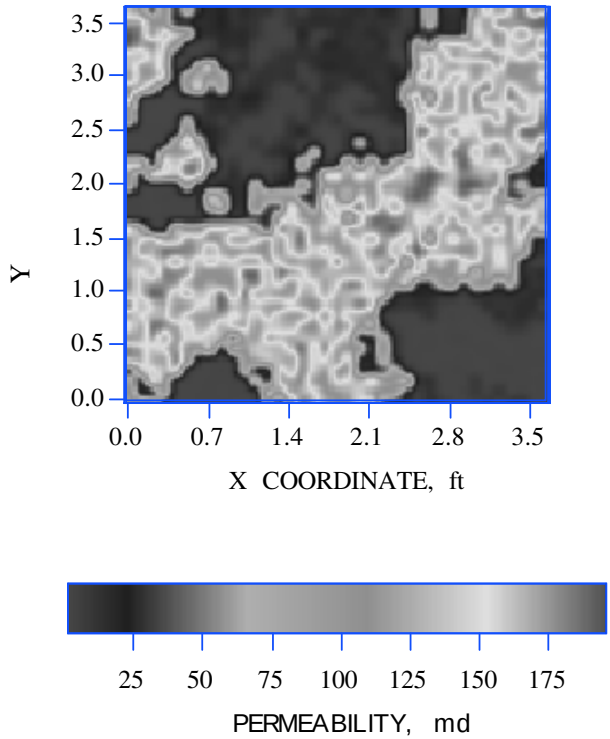


**Figure 3–4 Original Permeability Distribution for Three Lithologies Case**

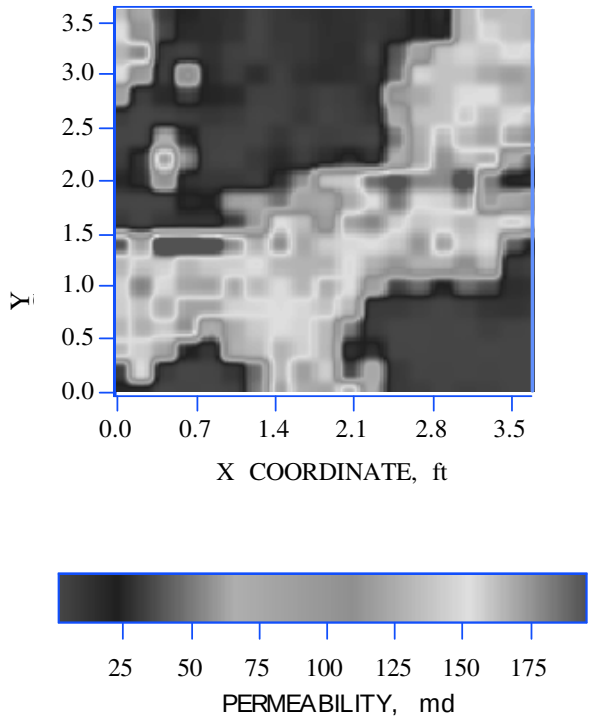


**Figure 3–5 Upscaled Permeability Distribution at Level 1 for Three Lithologies Case**

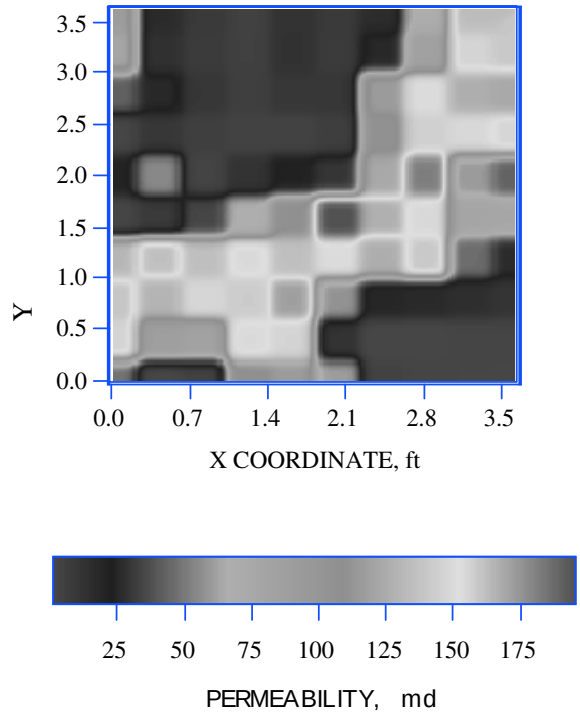


**Figure 3–6 Upscaled Permeability Distribution at Level 2 for Three Lithologies Case**

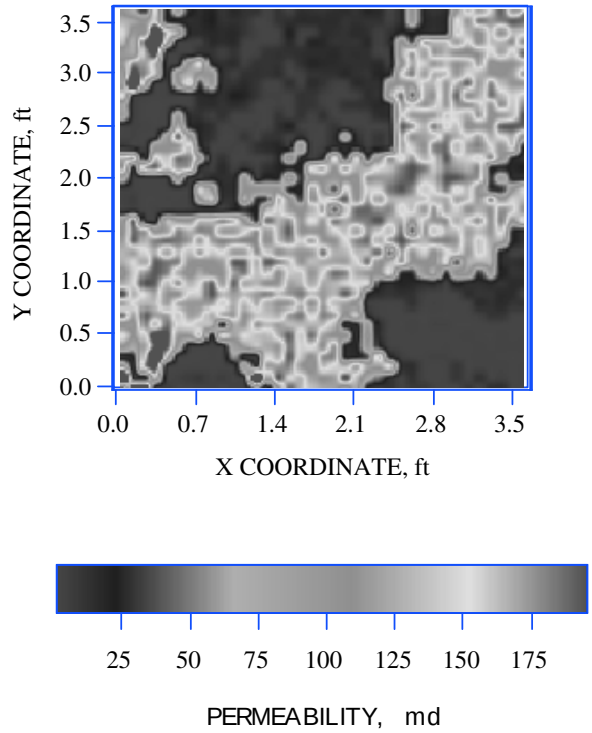


**Figure 3–7 Reconstructed Permeability Distribution for Three Lithologies Case**

# 4.0 WAVELET ANALYSIS FOR TWO-PHASE FLOW

Upscaling properties for multiphase flow is much more complicated than that for single-phase flow. Unlike the case of single-phase flow, where only absolute permeability affects the steady-state flow behavior, the flow properties for each phase and phase pressure difference within each geological facies and, probably more important, the rock-fluid property contrasts between the facies will also play a vital role for multiple lithologies and multiphase flow situations. Therefore, besides effective absolute permeability as in the case of single-phase flow, one needs to determine two additional equivalent properties: effective relative permeabilities and effective capillary pressure for the coarse-scale grid model. Such equivalent properties are flow-regime sensitive, making the problem more complicated. It is well known that flow regime in a multiphase flow is determined by the relative ratio among three major driving forces: viscous force, gravitational force, and capillary pressure. Roughly speaking, such a relative ratio among various driving forces will depend on flow velocity, scale of heterogeneity, size of grid block, and fluid properties. Considering that flow velocity and heterogeneity in a reservoir are spatially and/or temporally varying, therefore the equivalent relative permeability and capillary pressure will generally be spatially and temporally dependent and cannot be constructed without reference to geological structure and dominant flow regime.

In this section we propose a new two-phase upscaling method based on wavelet analysis techniques which, in contrast to conventional multiphase upscaling methods, does not require fine-scale simulation because it moves effects of the fine scales into coarser scales by multiscale wavelet transforms. The procedure begins with a fine-scale system which is populated with porosity, absolute permeability, and rock-fluid properties, such as phase relative permeabilities and capillary pressures. The rock and rock-fluid properties may vary substantially among different lithologies. The first step of the procedure is to upscale absolute permeability, and then upscale the phase permeabilities and capillary pressure based on hypothesis of capillary pressure dominant and viscous flow dominant, respectively. The third step of the procedure is to average the two groups of generated phase permeabilities and capillary pressures corresponding to each hypothesis weighted by ratio of capillary-viscous forces. The final step is normalizing the upscaled phase permeabilities using upscaled absolute permeability to obtain scaled-up relative permeabilities. The following sections will first present each step in detail and then present application examples under various geological contexts.

## 4.1 Upscaling Two-Dimensional Absolute Permeabilities

For a given fine-scale absolute permeability distribution, one can arrange the block permeability as a matrix,

$$K^0 = \begin{bmatrix} k_{1,1} & k_{1,2} & k_{1,3} & \cdots & k_{1,n} \\ k_{2,1} & k_{2,2} & \cdots & \cdots & k_{2,n} \\ k_{i,1} & \cdots & k_{i,j} & \cdots & k_{i,n} \\ k_{m,1} & \cdots & \cdots & \cdots & k_{m,n} \end{bmatrix} \tag{4–1}$$

where $k_{i,j}$ represents absolute permeability for block, and $i,j$ are the indexes for rows and columns, respectively. The superscript $0$ for matrix $K$ indicates that one assumes the original permeability distribution as a discrete approximation at scale $0$.

The implementation presented in this report is only interested in equivalent properties at coarser scale, and does not intend to use information carried by the detailed signals. Therefore, one can simplify the procedure proposed by Mallat (1989a). Generally speaking, one only need to convolute the permeabilities along one direction with low-pass filter first, followed by a convolution application using the same filter to the permeabilities along another direction.

For a chosen wavelet function, the filter matrix can be constructed from the coefficients of the basis function. For all the examples given here, a standard Daubechies filter, $D_4$, is used (Wickerhauser 1993). The following is the general makeup for the low-pass filter matrix for a four coefficients basis function that has a scale-to-scale relationship of 2.

$$H_{L,L/2} = \begin{bmatrix} h_1 & h_2 & h_3 & h_4 & 0 & 0 & 0 & 0 & \cdots & 0 & 0 \\ 0 & 0 & h_1 & h_2 & h_3 & h_4 & 0 & 0 & \cdots & 0 & 0 \\ 0 & 0 & 0 & 0 & h_1 & h_2 & h_3 & h_4 & \cdots & 0 & 0 \\ . & . & . & . & . & . & . & . & . & . & . \\ h_3 & h_4 & 0 & 0 & 0 & 0 & 0 & 0 & \cdots & h_1 & h_2 \end{bmatrix} \tag{4–2}$$

Notice that the dimension of the column for the dimension of the matrix $H$ is always twice as large as that of the row. For clarity in multiresolution analysis, from now denote a matrix $X$ with dimension $L \times n$ at scale level $m$ as $X^m_{L,n}$. Using this notation, a decomposition of permeability distribution at scale level $0$ along $j$ direction can be written as

$$\left(K^1_{L/2,n}\right)^j = H_{L/2,L} K^0_{L,n} \tag{4–3}$$

Note that the number of permeability values along $j$ direction is reduced by a factor of 2 after the above decomposition. The final permeability matrix at scale level $1$ can be determined by decomposing the resulting intermediate permeability matrix $\left(K^{1}_{L/2,n}\right)^{j}$ along $i$ direction in a similar manner,

$$K^{1}_{L/2,n/2} = \left\{ H_{n/2,n} \left[ \left( K^{1}_{L/2,n} \right)_{j} \right]^{T} \right\}^{T} \tag{4–4}$$

Combining Equations (4–3) and (4–4), a recursive procedure can be constructed to compute equivalent absolute permeability values at an arbitrary coarser scale $m$ from information at finer scale $m-1$ as follows:

$$K^{m}_{L/2,n/2} = H_{L/2,L} K^{m-1}_{L,n} \left( H_{n/2,n} \right)^{T} \tag{4–5}$$

Note that after one level decomposition, the dimension of the system and accordingly the number of the permeability values are reduced by a factor of 4. The above procedure can be generalized for decomposing any 2D data set by denoting the matrix, $K$, as a corresponding properly ordered data matrix.

## 4.2 Upscaling of Relative Permeabilities and Capillary Pressures

To avoid fine grid simulation, consider a steady-state incompressible, immiscible flow of water and oil in a heterogeneous permeable system which may consist of multiple geological facies. Further, assume rock-fluid properties within different facies may be substantially different so that saturation and capillary pressure discontinuities may exist between different facies. It is realized that the equivalent rock-fluid properties for coarser grids are not only a function of the spatial arrangement of the geological structure but also sensitive to relative ratios among driving forces within the flow medium system. In the following sections, the procedure is discussed in detail.

### 4.2.1 Normalizing Saturation

Suppose there are n types of rock-fluid properties, i.e., n sets of relative permeability curves and capillary pressure curves. First normalize saturation for each set of curves by

$$S_{1Di} = \frac{S_{1i} - S_{r1i}}{1 - S_{r1i} - S_{r2i}}, \qquad i = 1,2,\cdots,n \tag{4–6}$$

where subscript 1 represents water phase and 2 represents oil phase.

### 4.2.2 Determining Saturation Distributions

Saturation distributions are determined based on the hypothesis of flow regime made. When the flow regime is viscous dominated where capillary pressure number is small, water saturation distribution is controlled by viscous force and can be estimated from fractional flow curves, i.e.,

$$S_{1Di,v} = f_i^{-1}(f_i). \tag{4–7}$$

On the other hand, saturation distribution can be determined by capillary pressure while the flow is capillary pressure dominated,

$$S_{1Di,c} = P_{ci}^{-1}(P_{ci}). \tag{4–8}$$

### 4.2.3 Upscaling Saturation

Equivalent saturation for coarser scale blocks are determined by arithmetic average weighted by pore volumes as:

$$\bar{S}_{1D} = \frac{\sum_m V_{pi} S_{1Di}}{\sum_m V_{pi}} \tag{4–9}$$

where $m$ is the number of the finest grid blocks contained in each final coarsest scale block.

### 4.2.4 Upscaling Capillary Pressures and Phase Permeabilities

For each generated saturation distribution from Equation 4–7 or Equation 4–8 depending on the assumed flow regimes, one can determine the corresponding phase relative permeabilities and capillary pressures for each fine-scale grid from the sets of rock-fluid curves, and then compute phase permeability distributions for fine-scale system by multiplying the resulting relative permeabilities by corresponding absolute permeability. For each property distribution, construct the property matrix as was done in Section 4.1 and upscale the property for coarser scale using Equation 4–5. By this method, one can determine the phase permeabilities and capillary pressures for coarser scale corresponding to viscous-dominated and capillary pressure dominated flow regimes, respectively. For easy reference, denote them here by $(\bar{k}_{jv})_i, (\bar{k}_{jc})_i, (\bar{P}_{cv})_i$ and $(\bar{P}_{cc})_i$, respectively. Here, the subscripts $v$ and $c$ are used to denote viscous and capillary pressure dominated, respectively.

### 4.2.5 Weighting the Capillary Pressures and Phase Permeabilities

In the above sections, the equivalent properties have been determined for each coarser block for two extreme flow regimes, namely, viscous dominated and capillary-pressure dominated. The "true" equivalent properties can be approximated by a weighted average of above two extremes (Li et al. 1995).

$$\left(\bar{k}_j\right)_i = (1-\alpha)\left(\bar{k}_{jv}\right)_i + \omega\left(\bar{k}_{jc}\right)_i \tag{4–10}$$

and

$$\left(\bar{P}_c\right)_i = (1-\alpha)\left(\bar{P}_{cv}\right)_i + \omega\left(\bar{P}_{cc}\right)_i \tag{4–11}$$

where weighting factor is a function of capillary number, $N_{pc}$, and can be computed as follows:

$$\alpha = \frac{\log N_{pc} + 4}{5} \qquad \text{for } -4 \le \log N_{pc} \le 1. \tag{4–12}$$

### 4.2.6 Upscale Relative Permeabilities

To obtain the scaled-up relative permeabilities, simply divide the resulted scaled-up phase permeabilities by corresponding scaled-up absolute permeability, i.e.,

$$\left(\bar{k}_{rj}\right)_i = \frac{\left(\bar{k}_j\right)_i}{\bar{k}_i} \tag{4–13}$$

where subscript $j = w,o$ represents phase, and $i$ represents grid index of coarser scale system.

## 4.3 Application Examples

The proposed upscaling procedure using wavelet analysis has been tested in fine grid flow descriptions generated by a geostatistical simulation based on absolute permeability measurements from the Almond outcrop. Waterflooding simulations are run on Computer Modeling Group (CMG) Imex95 black-oil simulator. Numerical tests consisted of the following steps:

1. Injecting water under constant rate or constant pressure at one end of the system using a fully penetrated well, and then record the water and oil production histories from fully penetrated producing well at another end of the system for original find scale system using original rock and rock-fluid properties.
2. Use the same settings and simulation procedures on the upscaled flow system which was generated by the procedure described in previous sections.

3. Compare the two simulation results.

### 4.3.1 Geological Constraint on Outcrop Permeability Mapping

In order to characterize the lateral and vertical distribution of porosity and permeability within tidal-channel, tidal-delta, and foreshore facies, core plugs were taken from Almond outcrops located immediately north of Highway 430, Sweetwater County, Wyoming. The foreshore samples included both beach and swash bar components. More than 1,000 plugs 1 inch in diameter and up to 6 inches long were collected using a gasoline-powered motor and air-cleaned diamond-impregnated core bits. Horizontal and vertical (stratigraphic) coordinates were recorded for all samples, and the sample locations were correlated to a large strike-oriented stratigraphic cross section of the outcrop (Figure 2-2 from Chang et al. 1994). The distribution of major bedsets within tidal-channel (see Fig. 4–1) and tidal-delta facies (see Fig. 4–2) was determined using a series of photomosaics and observations recorded in the field. A map of the distribution of permeability within the bottom 5 ft of the tidal delta facies (see Fig. 4–3) shows that permeability trends within major bedsets tend to follow the overall depositional "grain" as delineated by the cross bedding direction, that permeability changes quite rapidly in the vertical direction, and that the permeability trends are often truncated at bedset boundaries.

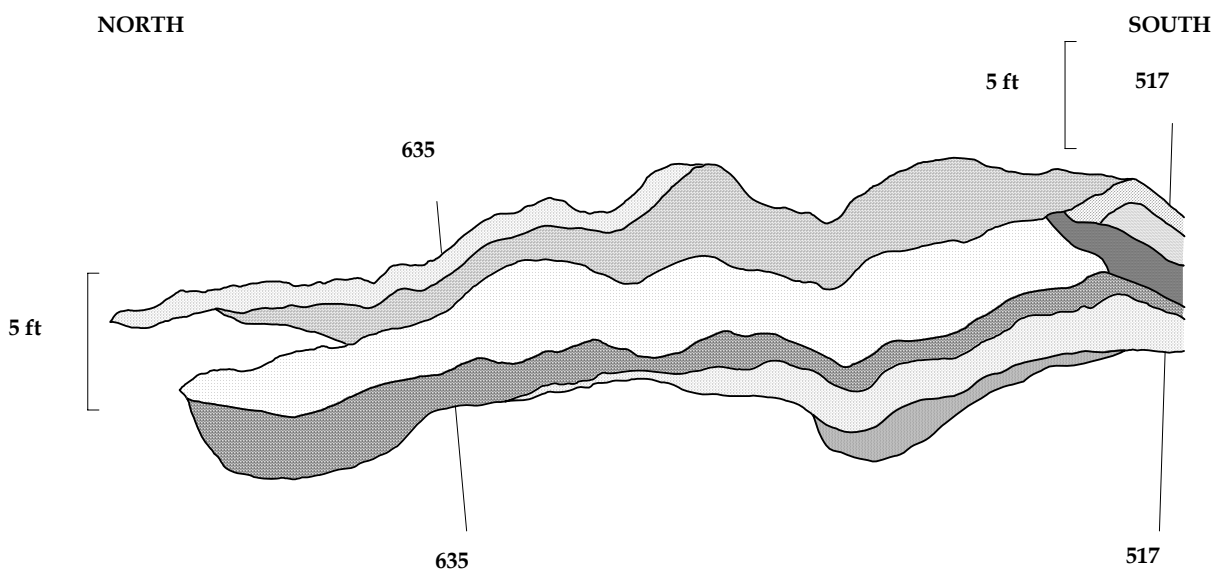


**Figure 4–1 Almond Formation Outcrop G Tidal-Channel 1 Bedset Boundaries. Datum is base of outcrop; 517 and 635 represent distance in feet north of the southernmost extent of the outcrop. Figure was reconstructed from an outcrop photomosaic.**

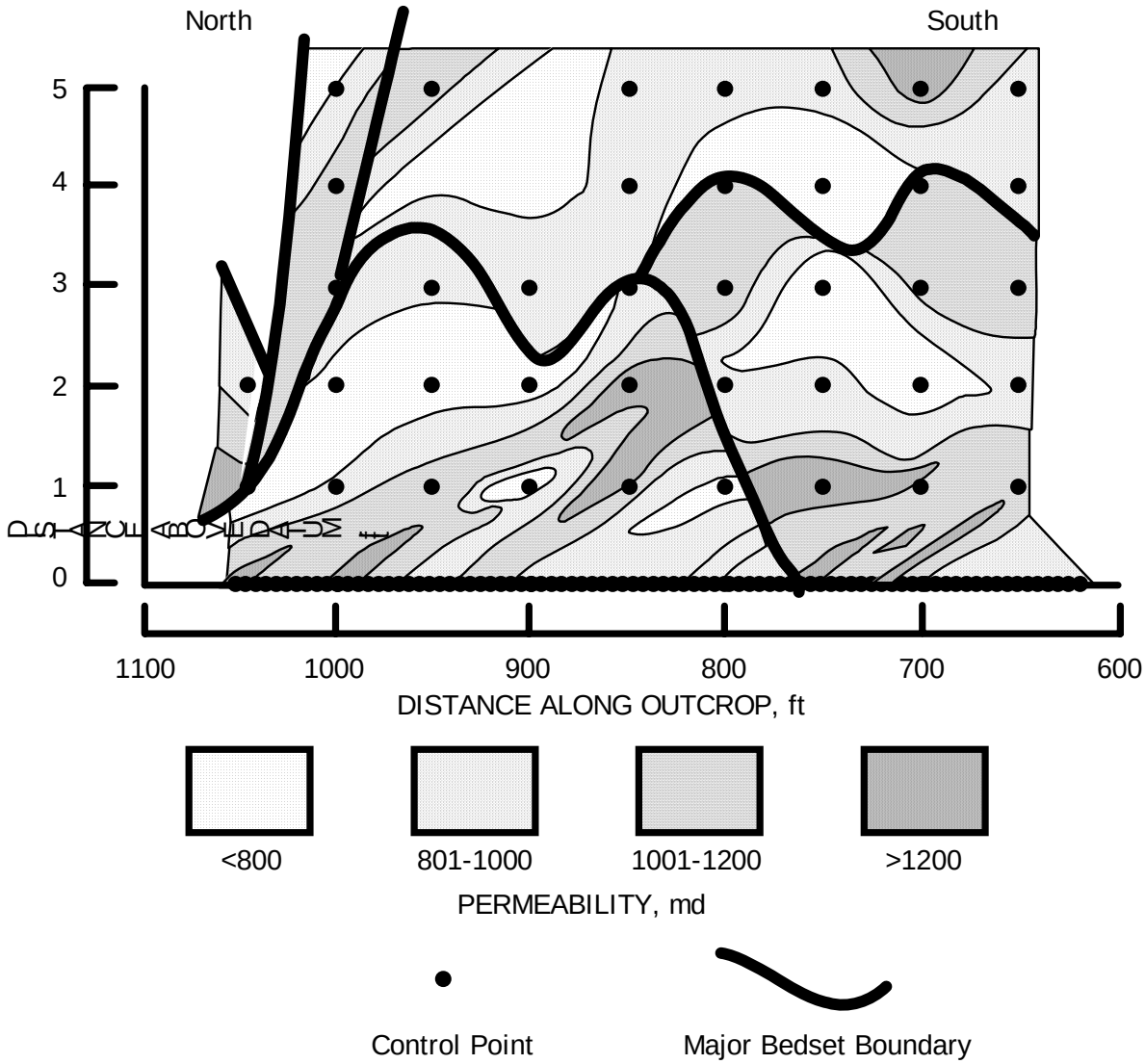


**Figure 4–3 This Figure Is a Reconstruction of the Geologically Constrained Distribution of Permeability within the Bottom 5 ft of the Tidal Delta Whose Major Bedsets Are Outlined in Figure 4–2. Note the northward dip and rapid changes of permeability in the vertical direction. Extreme vertical exaggeration causes the major bedset boundaries to assume a sinusoidal geometry.**

Medium-scale geological constraints (including major bedset distribution, the direction and thickness of cross bedding, and the degree of preservation of the major bedforms) to a large extent determine the trend and complexity of the interfacies permeability distribution which could not be accurately modeled in the absence of such data.

The foreshore facies consisted of 90% thin-bedded, parallel-to-subparallel lamination typical of a beach setting. Major bedsets were not distinguished within this facies except for a 1-ft-thick

planar cross-laminated bed representing an accreting spit or a shoreline-welded tidal swash bar. Detailed sampling from this interval allowed us to reconstruct the fine-scale variations of permeability within the planar cross-laminated unit Figure 4–4. Cross lamination and the trend of the permeability dips toward the north in a pattern that is both very fine in scale and is strongly controlled by the bedding. The fine-scale distribution of permeability can only be mapped with a detailed knowledge of the geological constraints that here consist of monotonously northward-dipping cross lamination. It should be noted that the top of the bedform has generally greater permeability than the bottom of the bedform and that thin high permeability "streaks" dip northward into the bedform parallel to the cross lamination.

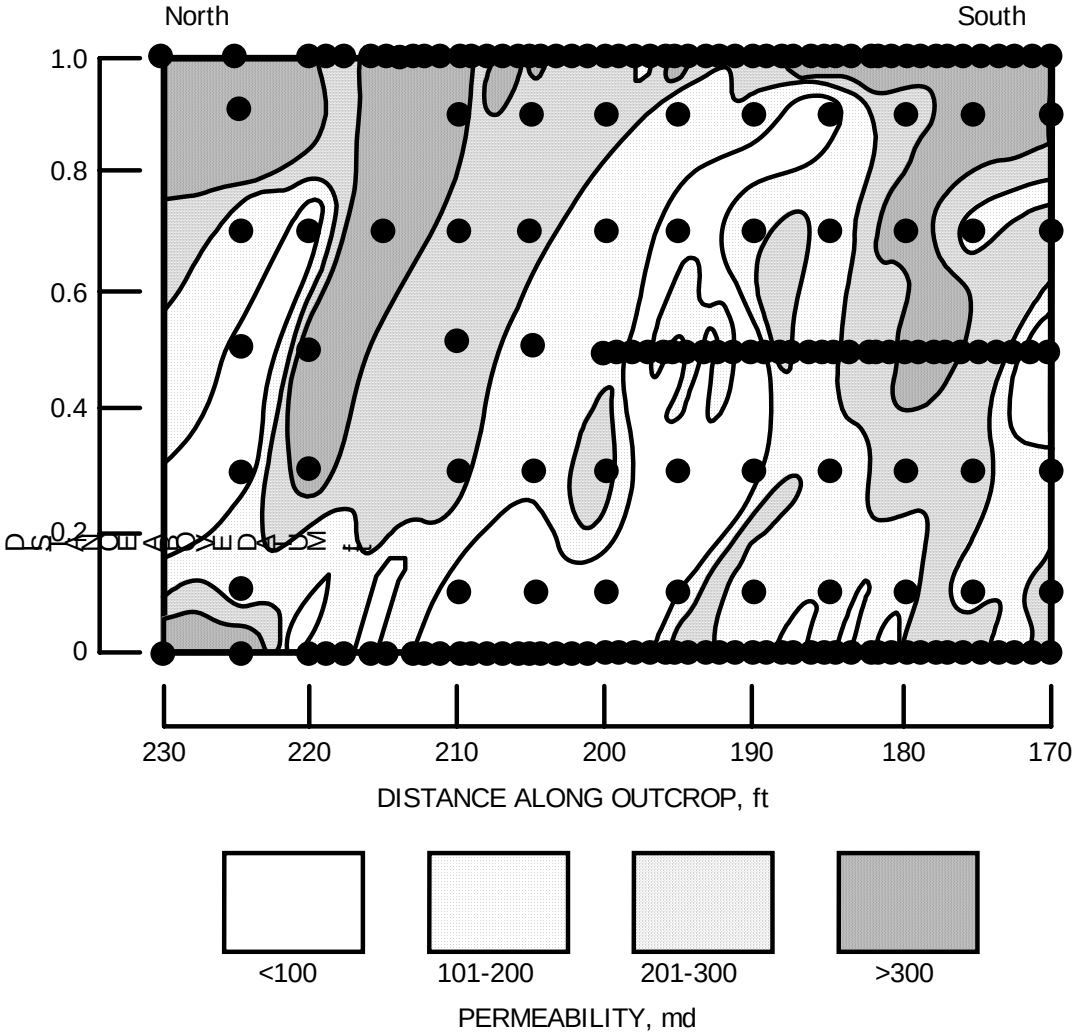


**Figure 4–4 Closely Spaced Core Plug Samples from a 1-ft-Thick Northward Dipping, Planar Cross-Bedded Tidal Swash Bar within the Foreshore Facies Illustrate the Fine Detail of Permeability Variations within the Bedset and That Is Parallel to the Bedding Direction. Individual Sandstone Laminae are Less than 1 cm Thick.**

The distribution of data from two tidal channels did not lend itself to valid mapping of permeability within the bedsets. The bedset units tend to be thin within the tidal channels (typically less than 2 ft thick) and usually only a single value was taken from a unit at any distance along the outcrop. Permeability among bedsets for the two tidal channels can be compared in Tables 4–1 and 4–2. Data from these tables indicates that permeability for the bottom-most bedset in each tidal-channel deposit is significantly greater than other bedsets from a given tidal channel. The average permeability for the upper bedsets from each tidal channel, as a whole, are similar, with the average for all bedsets in tidal channel 2 about twice that from tidal channel 1. Based on these data, the major tidal-channel bedsets should be modeled with a high permeability base and a lower permeability upper region where absolute permeability values average only a few hundred md.

**Table 4–1 Comparison of Permeability between Major Bedsets within Tidal Channel 1**

| Bedset Number | Mean Permeability | Range | Standard Deviation | Number of Points |
|---|---|---|---|---|
| 5 (Bottom) | 835.2 | 428.9–1570.2 | 332.9 | 9 |
| 6 | 199.6 | 17.8–825.5 | 148.0 | 43 |
| 7 | 123.2 | 3.5–574.5 | 87.5 | 139 |
| 8 (Top) | 170.9 | 45.2–348.5 | 99.5 | 13 |
| All Bedsets | 173.1 | | | |

**Table 4–2 Comparison of Permeability between Major Bedsets within Tidal Channel 2**

| Bedset Number | Mean Permeability | Range | Standard Deviation | Number of Points |
|---|---|---|---|---|
| 18 (Bottom) | 612.6 | 546.3–678.9 | 93.7 | 2 |
| 19 | 229.1 | 132.8–287.1 | 49.2 | 7 |
| 20 | 250.9 | 40.1–1223.0 | 154.62 | 175 |
| 21 | 237.7 | 117.5–726.4 | 220.1 | 7 |
| 22 | 271.8 | 87.7–680.6 | 151.3 | 36 |
| 23 | 256.1 | 69.4–443.8 | 108.2 | 19 |
| 24 | 335.0 | 137.7–770.5 | 171.9 | 22 |
| 25 (Top) | 306.7 | 110.0–486.4 | 142.2 | 6 |

| | |
|---|---|
| All Bedsets | 263.7 |

Average petrophysical properties are summarized for depositional facies in Table 4–3. Tidal channel and foreshore facies have a few hundred md average permeability with porosity ranging from 25% to 27%. Within the foreshore facies the swash bar/spit depositional setting has about half the permeability of the beach setting. Significantly greater petrophysical properties are present in the tidal delta facies where average permeability is greater than one Darcy and porosity is greater than 30%.

**Table 4–3 Average Petrophysical Properties for Horizontally Oriented Plugs**

| Facies | Average Ø, % | Average K, md | Number Samples |
|---|---|---|---|
| Beach | 27.1 | 421.8 | 172 |
| Swash Bar/Spit | 25.3 | 219.0 | 183 |
| All Foreshore (beach + swash bar) | 26.2 | 317.2 | 355 |
| Tidal Channel | 25.6 | 225.2 | 480 |
| Tidal Delta | 31.5 | 1036.6 | 144 |
| All Data | 26.8 | 377.9 | 979 |

All the measurements served as hard data points and were also used to infer statistical parameters which characterize the fine-scale variations within the tidal-delta, tidal-channel, and foreshore facies. Realizations of each facies were constructed using the LU (low up) conditional simulation constrained by all the a priori geological information. Using this method, all the realizations used for upscaling procedure will be in a more realistic geological context in that they honor all the hard data and statistical parameters inferred from outcrop measurements.

Using absolute permeability measurements from the Almond outcrop, we constructed semivariograms for tidal-channel, tidal-delta, and beach facies, which are shown in Figure 4–5, 4–6, and 4–7, respectively. The fitted variogram models are inserted in the figures, and logarithm means and logarithm variances for each facies are summarized in Table 4–4. Note that while tidal-channel and tidal-delta facies present a geometric anisotropy (semivariograms have one sill), the beach facies indicates a zonal anisotropy (semivariograms have two sills) (Kelkar 1990).

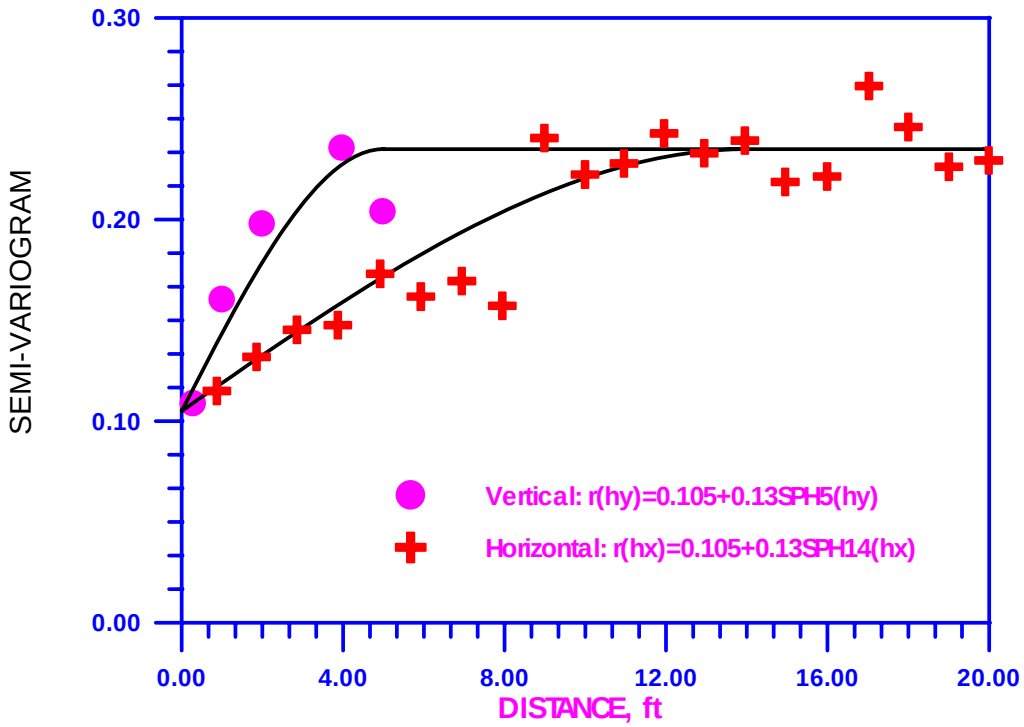


**Figure 4–5 Semivariogram of Permeability for the Tidal-Channel Facies**

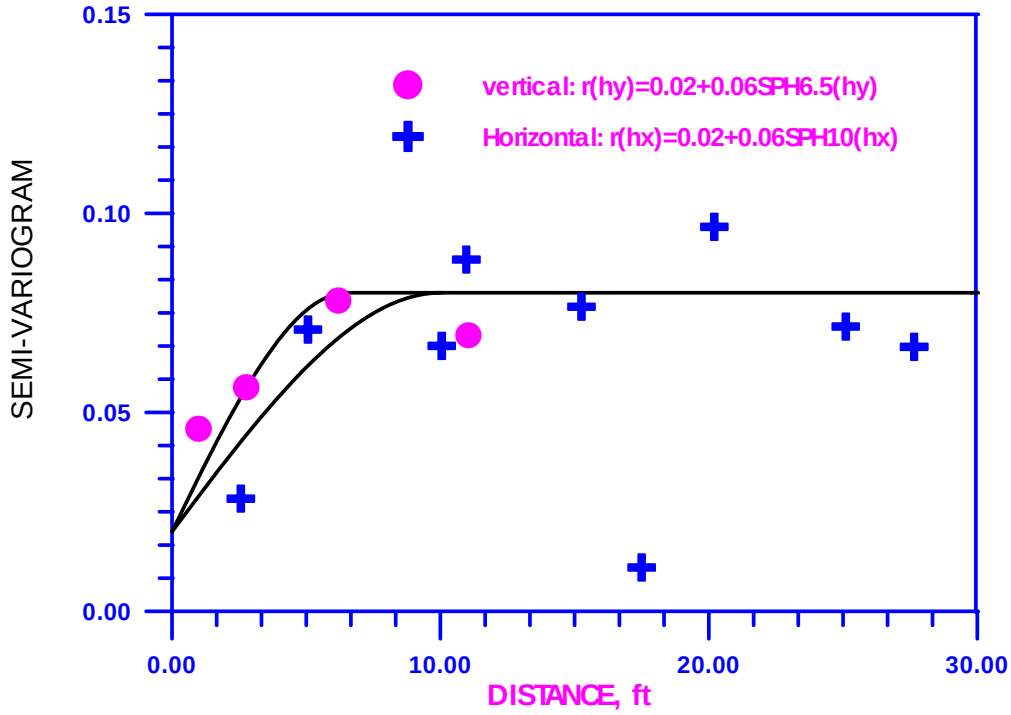


**Figure 4–6 Semivariogram of Permeability for Tidal-Delta Facies**

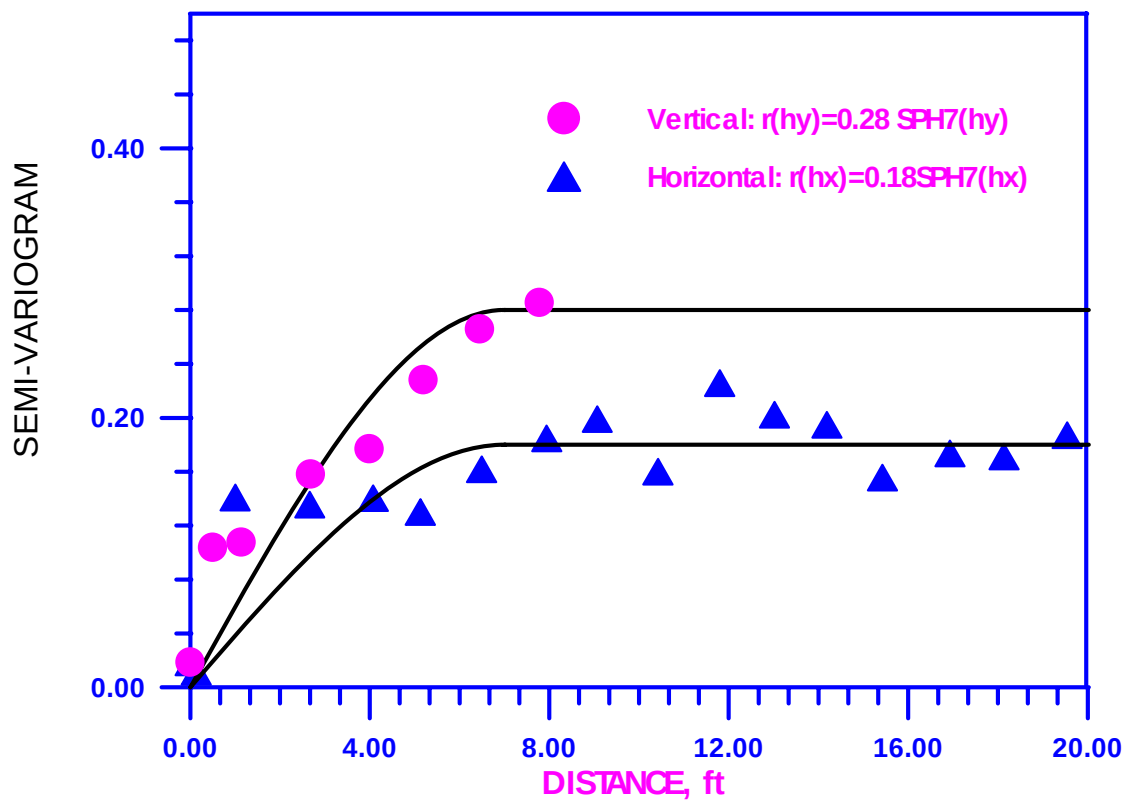


**Figure 4–7 Semivariogram of Permeability for Beach Facies**

**Table 4–4 Statistical Parameters of Facies**

| Parameters\Facies | Tidal-Channel | Tidal-Delta | Beach |
|---|---|---|---|
| Log Mean | 5.51 | 6.94 | 5.89 |
| Log Variance | 0.462 | 0.3 | 0.614 |

To accomplish geostatistical simulation, construct covariance matrix $C_M$ from normalized semivariogram models, $\gamma(h)$ (Kelkar 1990) by the following relationship,

$$C(h) = C_0 - \gamma(h) \tag{4–14}$$

The a posteriori covariance matrix after conditioning to all the hard data can be computed by (Chu et al. 1995b):

$$C_{mh} = C_M - C_M G_h^T (G_h C_M G_h^T + C_h)^{-1} G_h C_M \ . \tag{4–15}$$

Realizations honoring the semivariogram model and hard data can be generated from the following equation:

$$m_r = m_0 + LZ_r \tag{4–16}$$

where $m_0$ is mean of the model, $Z_r$ is a vector of independent normal deviates, and lower diagonal matrix, $L$, is determined by Cholesky decomposition of the a posteriori covariance matrix, $C_{Mh}$,

$$C_{Mh} = LL^T \tag{4–17}$$

The realizations for tidal-channel, beach, and tidal-delta facies on a $24 \times 56$ grid system with grid size of $0.5 \times 0.5 \times 0.5$ ft are shown in Figures 4–8, 4–9, and 4–10, respectively.

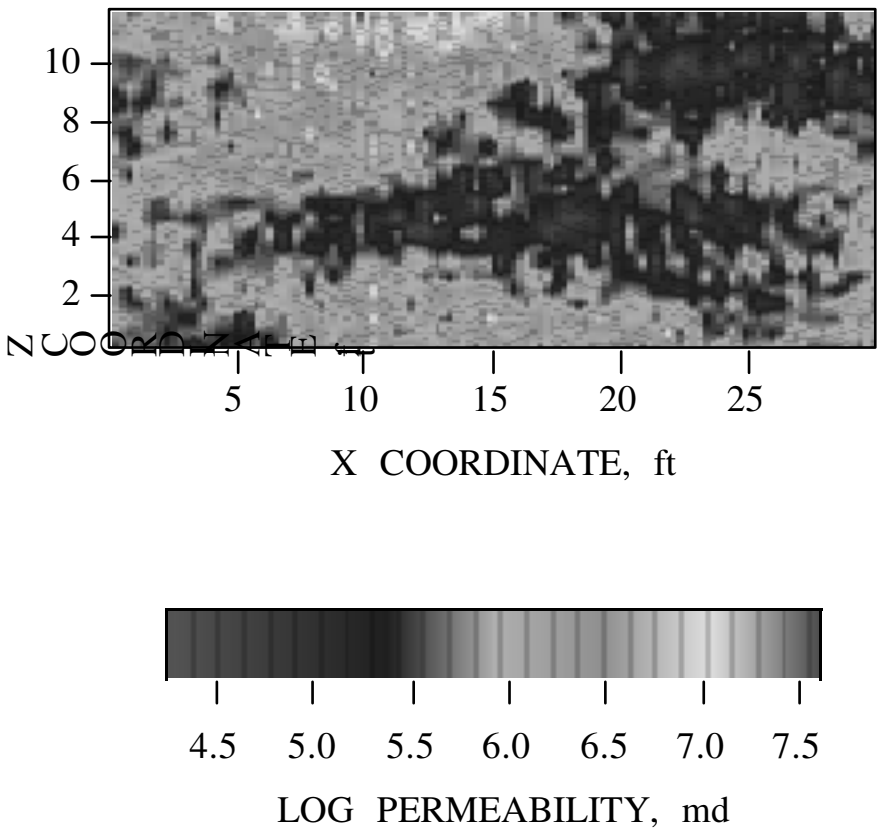


**Figure 4–8 A Realization of Permeability Distribution within the Tidal-Channel Facies Based on Outcrop Samples**

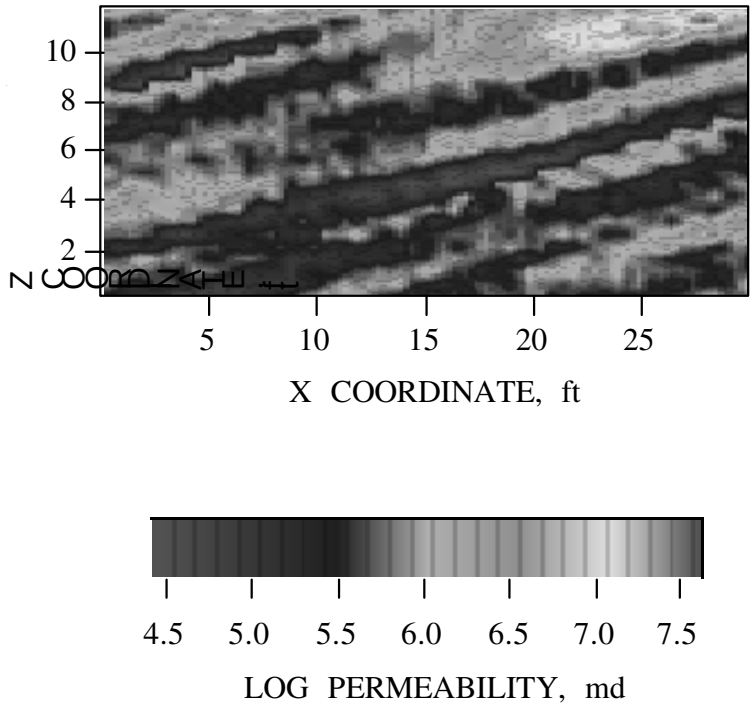


**Figure 4–9** **A Realization of Permeability Distribution within the Beach Facies Based on Outcrop Samples**

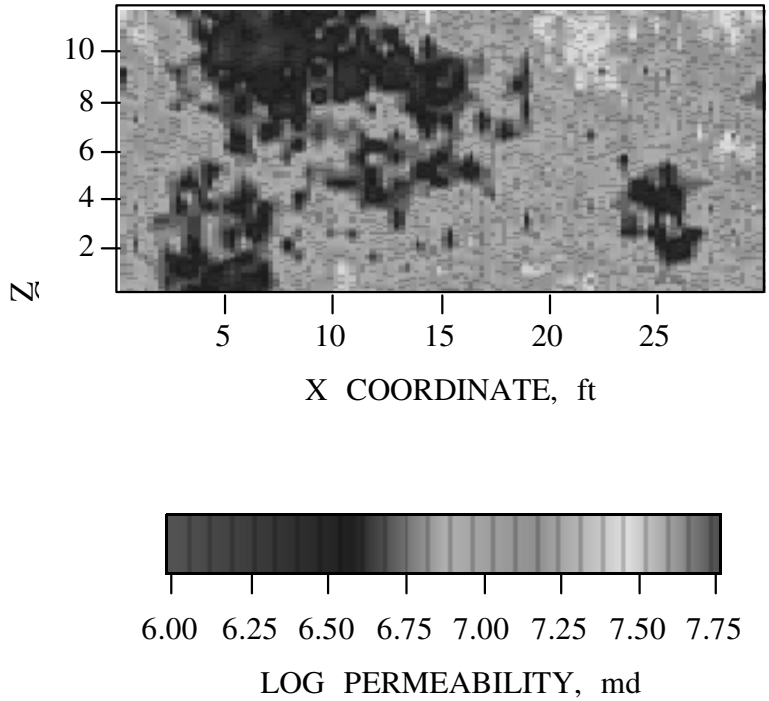


**Figure 4–10** **A Realization of Permeability Distribution within the Tidal-Delta Facies Based on Outcrop Samples**

### 4.3.2 Rock-Fluid Properties

We have used the following exponential forms of original rock-fluid properties for the flow modeling,

$$k_{r1}(S_{1D}) = k_{r1}^{0}(S_{1D})^{n1}, \tag{4–18}$$

$$k_{r2}(S_{1D}) = k_{r2}^{0}(S_{1D})^{n2} \tag{4–19}$$

and

$$P_c = p_c^0(1 - S_{1D})^{n_{pc}}. \tag{4–20}$$

Two types of relative permeability curves and capillary pressure curves, denoted as type 1 and type 2, are used for upscaling, and the associated parameters for them are given in Tables 4–5 and 4–6, respectively.

**Table 4–5 Parameters for Relative Permeabilities**

| Type No. | $S_{r1}$ | $S_{r2}$ | $n_1$ | $n_2$ | $k_{r1}^0$ | $k_{r2}^0$ |
|---|---|---|---|---|---|---|
| 1 | 0.37 | 0.18 | 4.0 | 1.5 | 0.1 | 0.84 |
| 2 | 0.25 | 0.26 | 3.25 | 2.25 | 0.23 | 0.81 |

* All the symbols used in this table are defined in Section 1.5, Nomenclature.

**Table 4–6 Parameters for Capillary Pressures**

| Type No | $S_{r1}$ | $S_{r2}$ | $n_{pc}$ | $P_c^0$ |
|---|---|---|---|---|
| 1 | 0.37 | 0.18 | 2.0 | 15.0 |
| 2 | 0.25 | 0.26 | 3.5 | 18.0 |

* All the symbols used in this table are defined in Section 1.5, Nomenclature.

### 4.3.3 Interbedset Upscaling

The absolute permeability realization for beach facies outcrop was evaluated using the proposed wavelet upscaling method. As shown clearly in Figure 4–9, there exist lower permeability beddings inserted in the relative high permeability background in the beach facies. Close examination also revealed crossbedding with about a 30° dip angle within the bedsets. After three levels of wavelet upscaling, the number of grids in the system was reduced from

1344 to 21 with a factor 64. Figures 4–11 and 4–12 compare oil production and water production, and water cut histories from simulations of the original and upscaled systems of beach facies, respectively. Here, type 2 rock-fluid properties in the simulations are used. The upscaled system, although with substantial reduction of grids, gives flow behavior which matches the fine grid system simulation almost perfectly. Considering that the beach facies presents the most difficult situation for upscaling among the three facies encountered (tidal-delta, tidal-channel, and beach), the above excellent results almost ensure, without further testing on the other two remain facies, that wavelet upscaling method is an efficient and accurate technique for upscaling interbedding properties. Nevertheless, similar flow simulation tests on the other two facies were still made. As expected, the upscaled system reproduced the production performances from the corresponding original system very well as demonstrated by Figures 4–13, 4–14, 4–15, and 4–16.

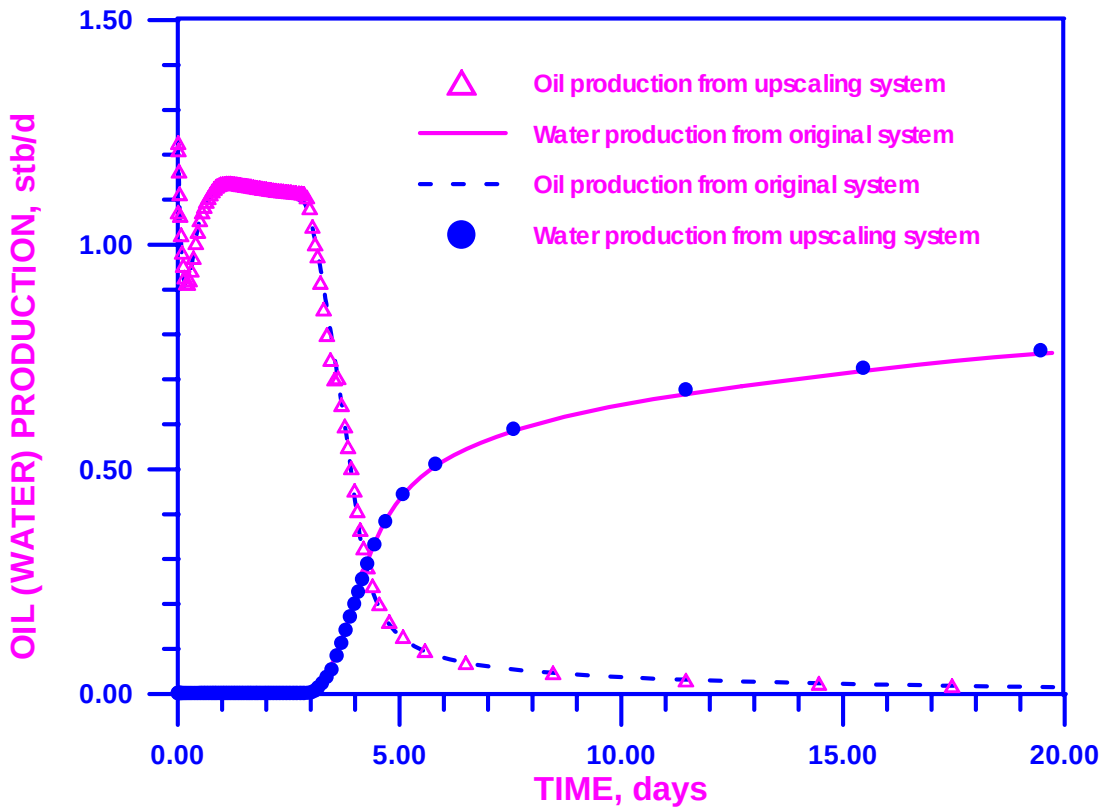


**Figure 4–11 Comparison of Production Performances from Original and Upscaling Systems (Beach Facies)**

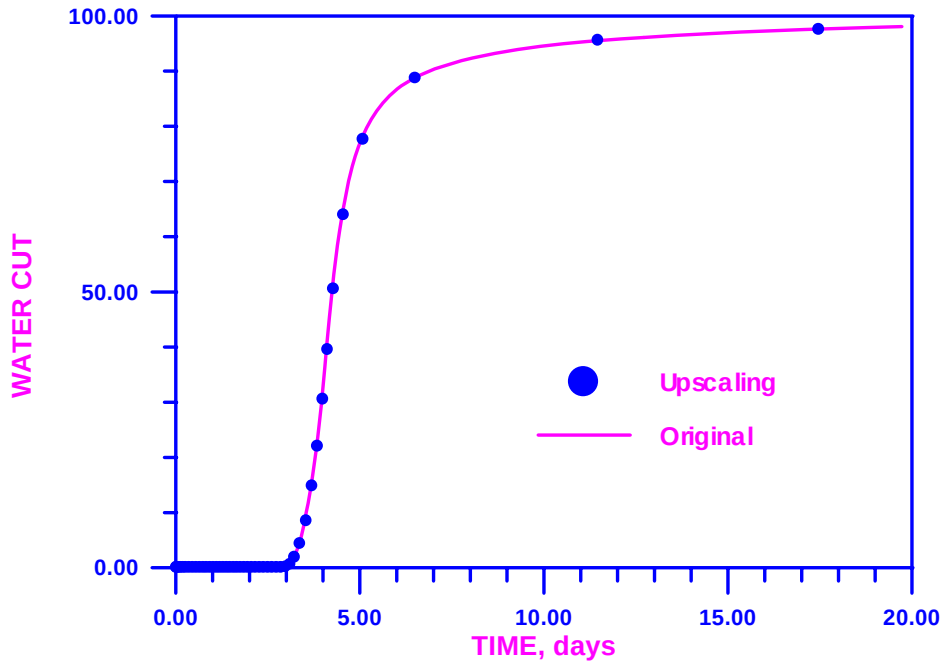


**Figure 4–12** Comparison of Water Cut at Production Wells from Original and Upscaling Systems (Beach Facies)

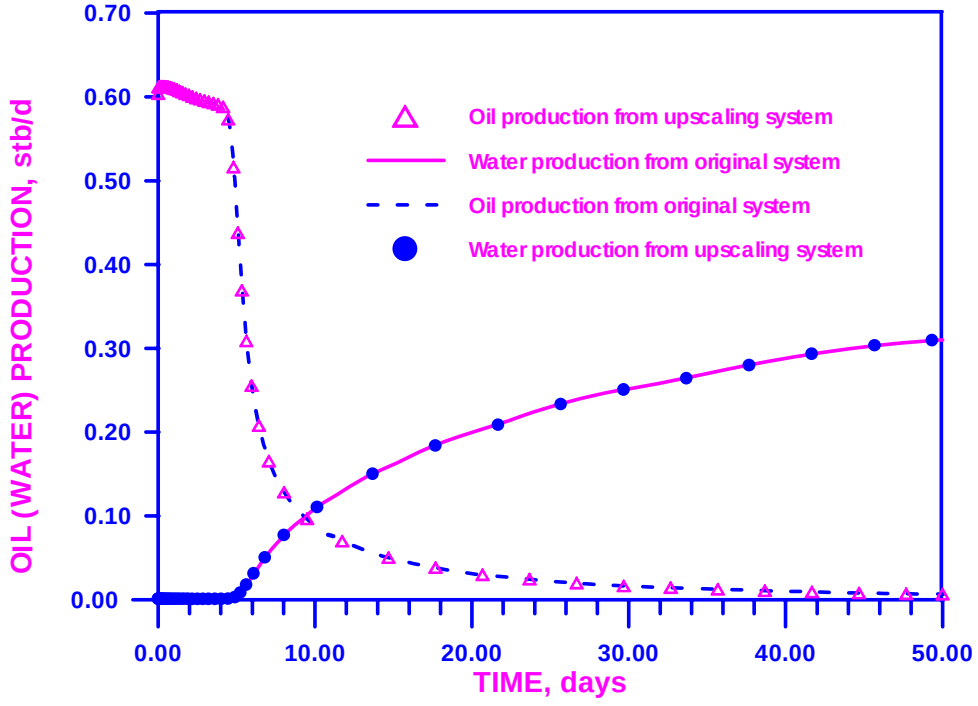


**Figure 4–13** Comparison of Production Performances from Original and Upscaling Systems (Tidal-Delta Facies)

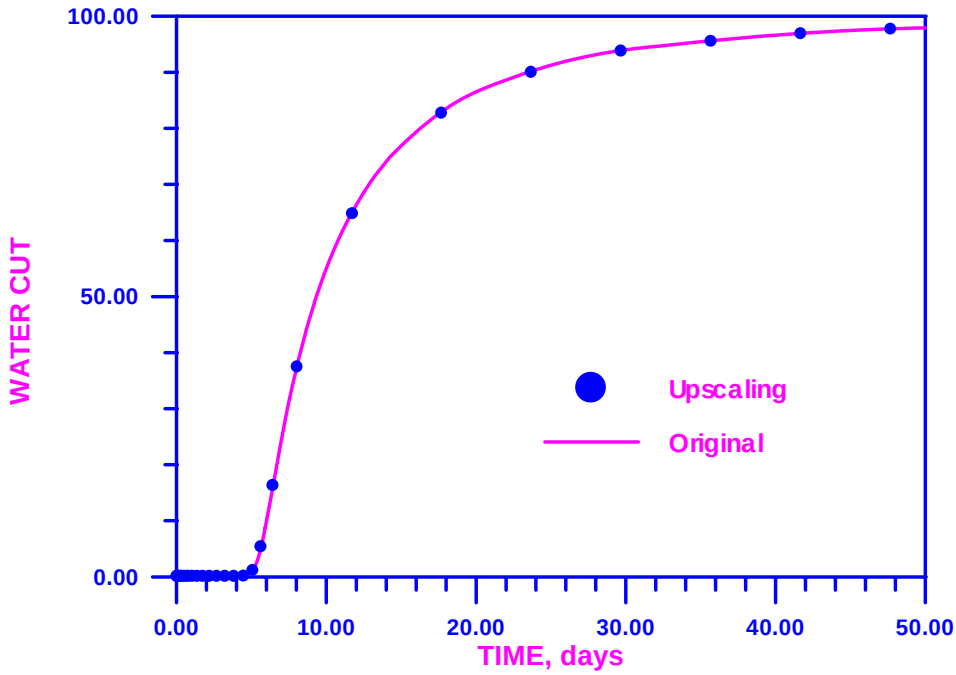


**Figure 4–14** **Comparison of Water Cut at Production Wells from Original and Upscaling Systems (Tidal-Delta Facies)**

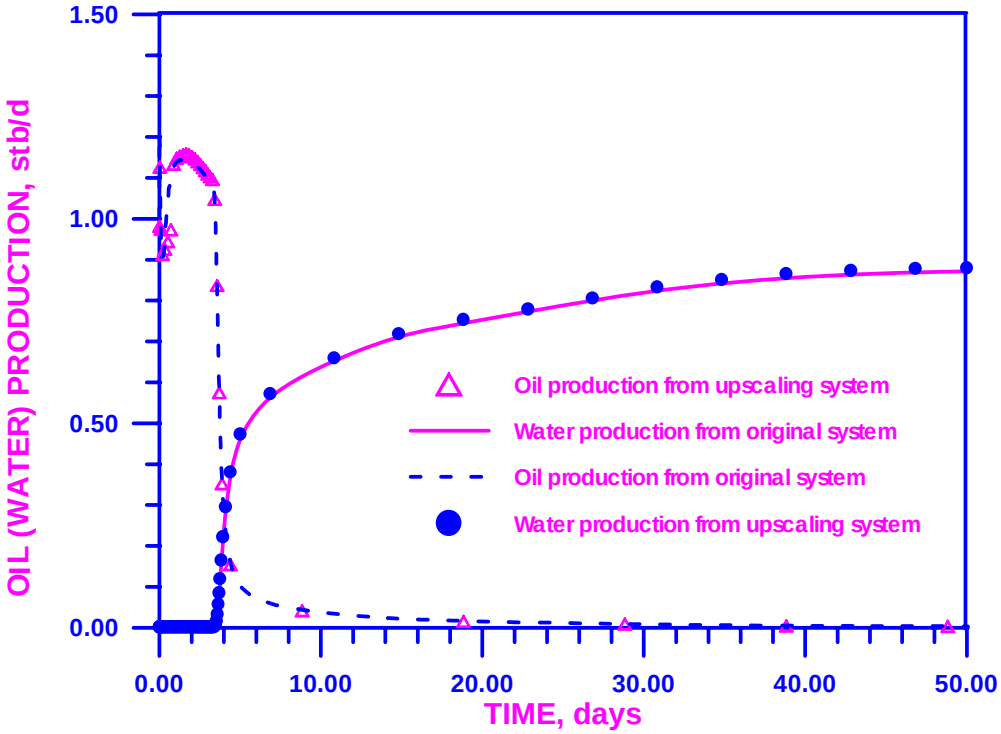


**Figure 4–15** **Comparison of Production Performances from Original and Upscaling Systems (Tidal-Channel Facies)**

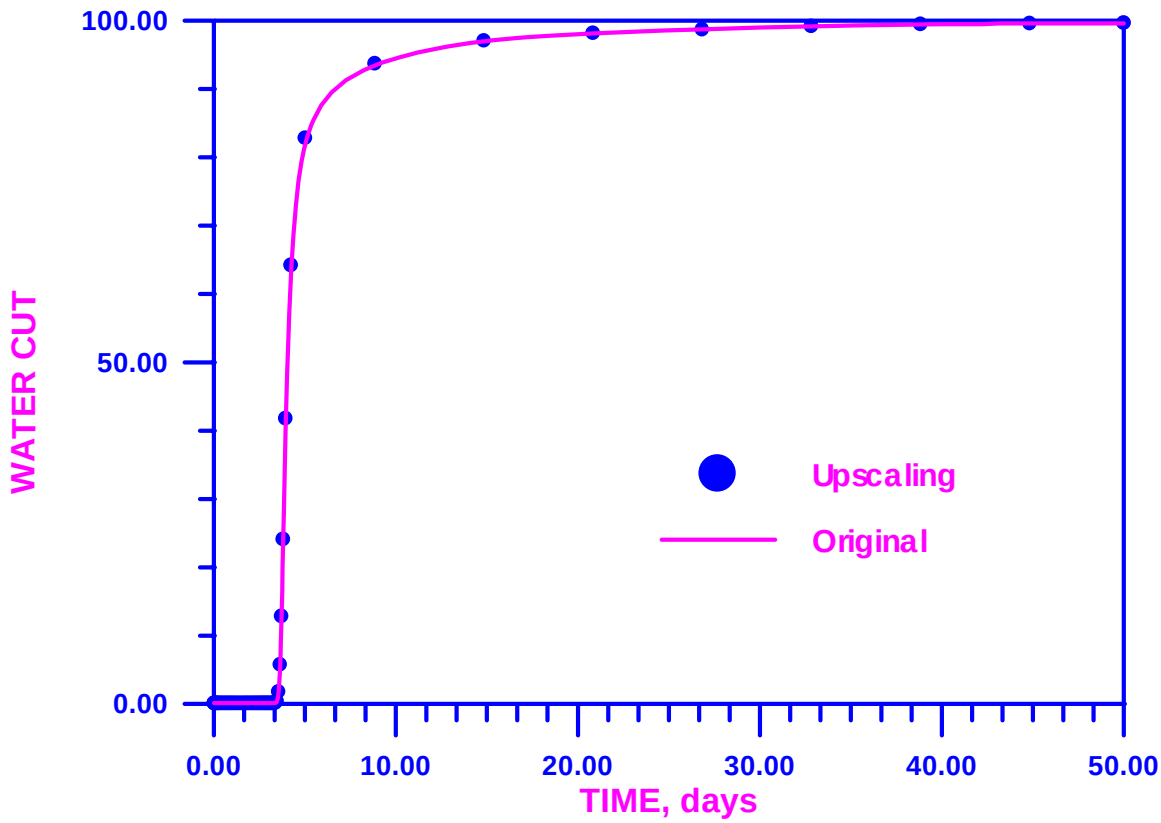


**Figure 4–16 Comparison of Water Cut at Production Wells from Original and Upscaling Systems (Tidal-Channel Facies)**

### 4.3.4 Interfacies Upscaling

To demonstrate the applicability of the newly developed wavelet upscaling method for a multiple facies system under multiphase flow conditions, we artificially constructed two-facies systems by combining parts of two different facies into one model. Two systems were constructed, one by combining beach and tidal-delta facies and another by combining tidal-channel and beach facies, as shown in Figures 4–17 and 4–18, respectively. As illustrated in Figures 4–17 and 4–18, the contrasting two facies contact each other along a diagonal line of the constructed rectangular systems.

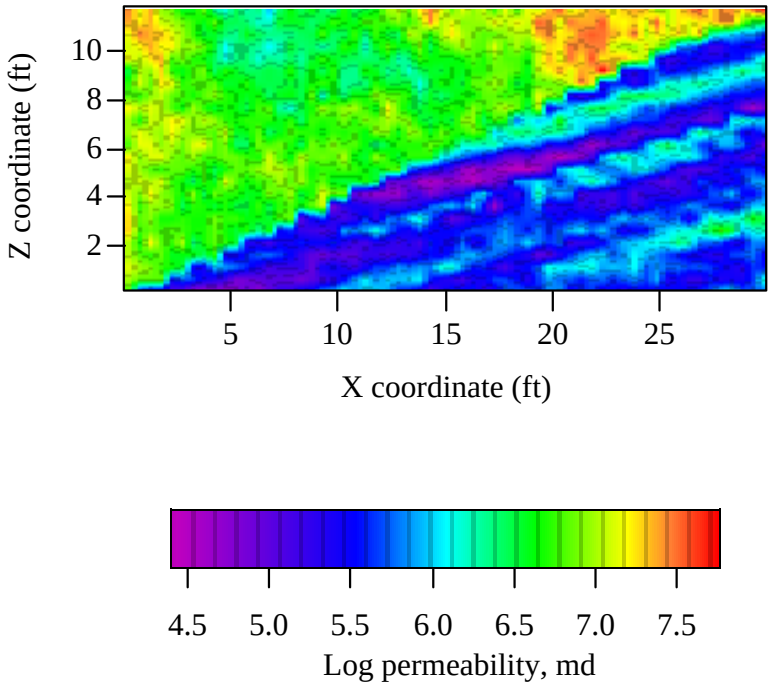


**Figure 4–17 A Realization of Permeability Distribution within the Tidal-Delta and Beach Facies Based on Outcrop Samples**

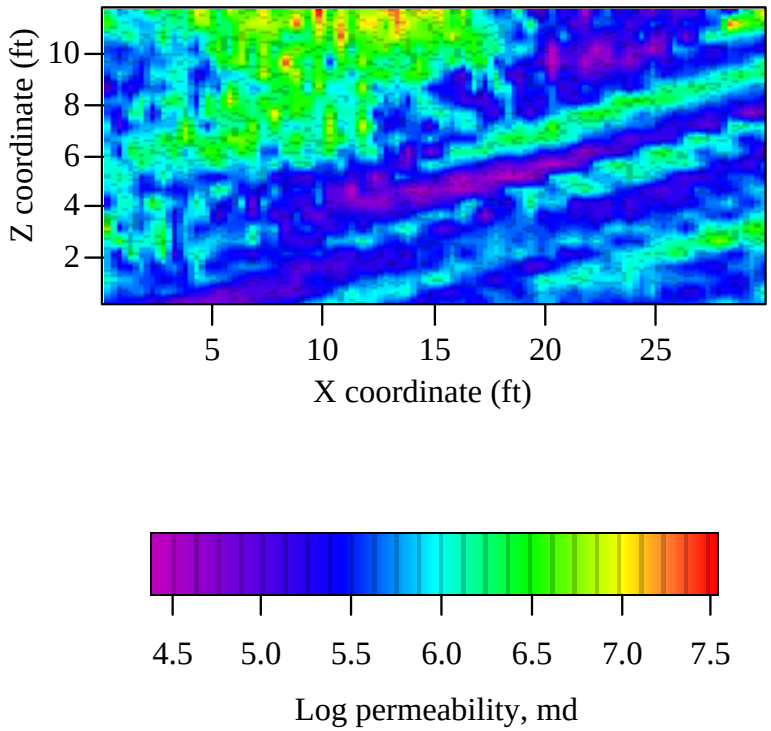


**Figure 4–18 A Realization of Permeability Distribution within the Tidal-Channel and Beach Facies Based on Outcrop Samples**

The first test was run on the tidal-channel and beach composite system and assumed type 1 rock-fluid properties for beach facies and type 2 for tidal-channel facies (refer to Tables 4–5 and 4–6). A constant injection rate (0.5 bbl/d) is imposed on a fully penetrated injector at one end of the system, and a constant pressure producer (2770 psi) produced oil and water at another end. Figures 4–19 and 4–20 show the comparison of the production performances from the original and upscaling systems. Although there are slight discrepancies between the water productions and water cuts from original and upscaled system after breakthrough, the breakthrough time, oil production history, and main characteristics of the water production history have been well captured.

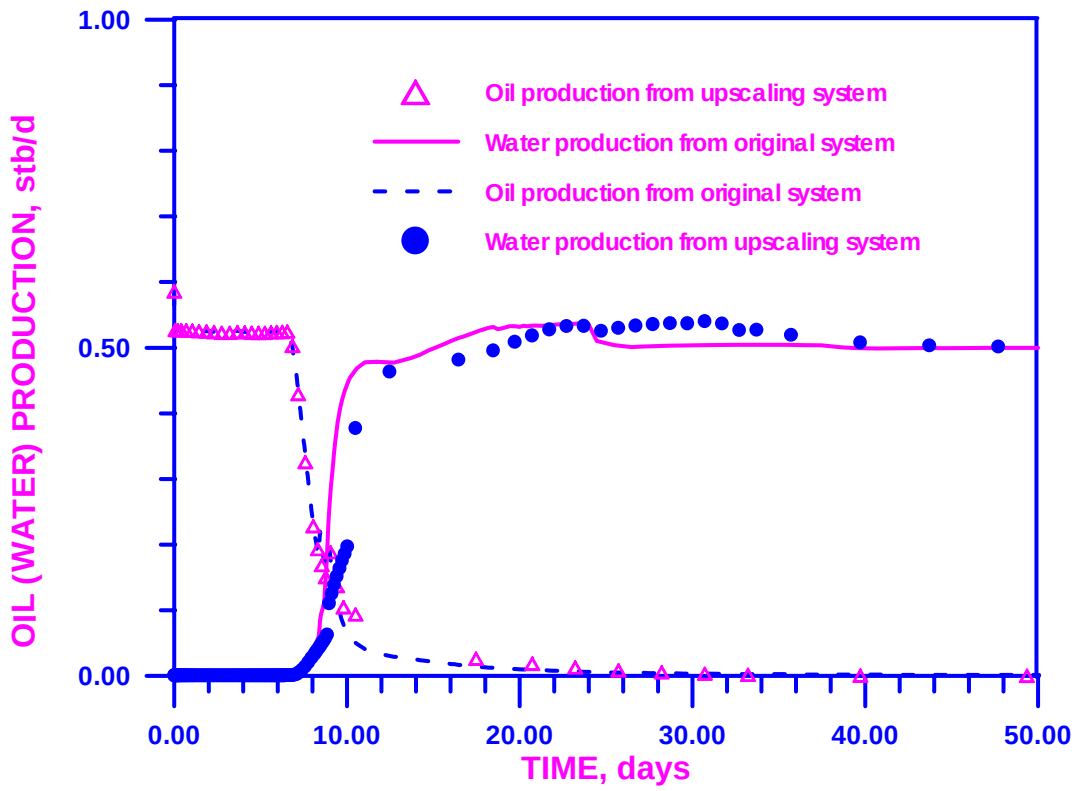


**Figure 4–19 Comparison of Production Performances from Original and Upscaling Systems (Tidal-Channel and Beach Composite System)**

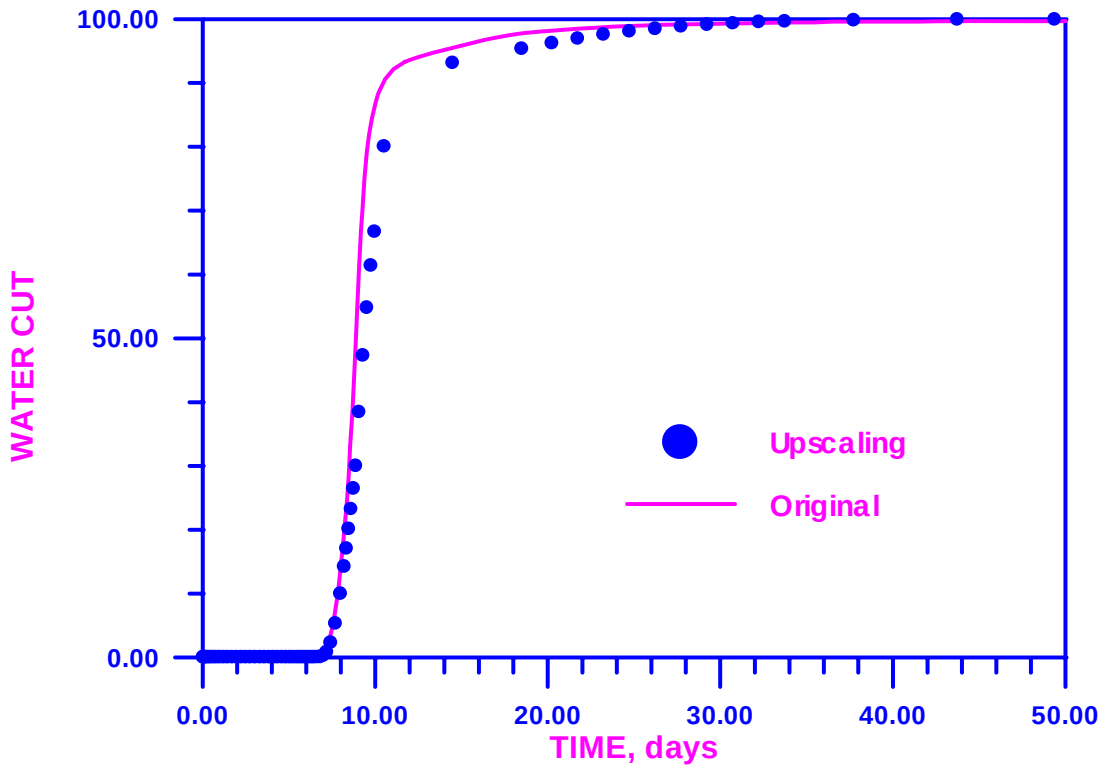


**Figure 4–20 Comparison of Water Cut at Production Wells from Original and Upscaling Systems (Tidal-Channel and Beach Composite System)**

The second test was run on tidal-delta and beach composite system. We assigned type 1 rock-fluid properties for beach and type 2 for tidal-delta facies. The simulation scheme is the same as for the previous example, except for changing the injector to a constant pressure well with a 2900-psi bottomhole pressure. As shown in Figures 4–21 and 4–22, the production histories of the original system were well reproduced by the upscaled system.

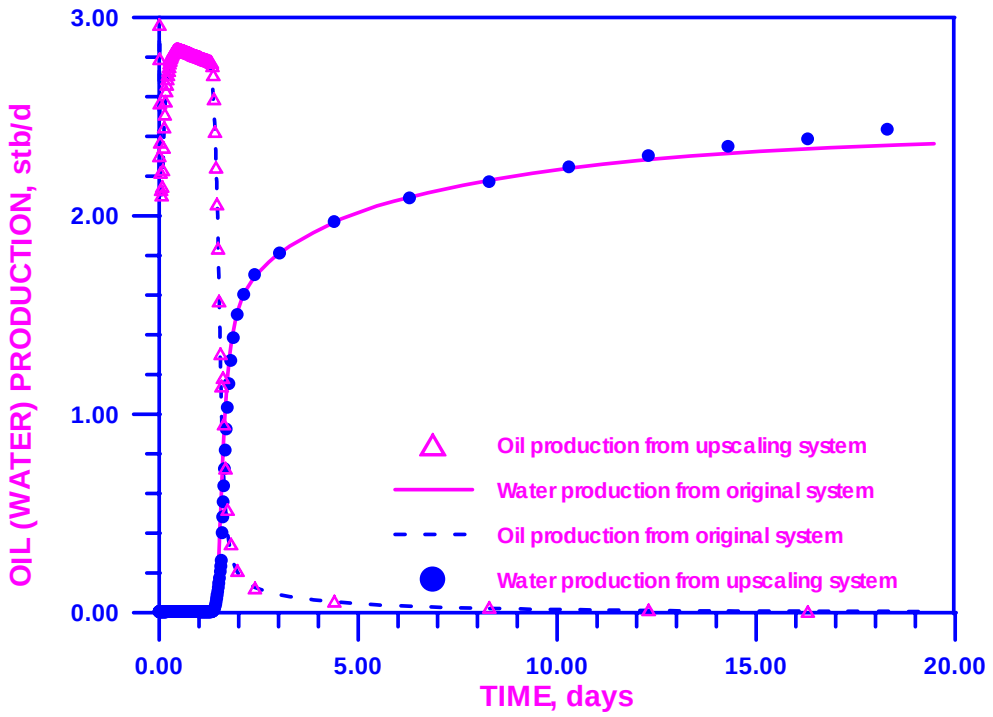


**Figure 4–21** Comparison of Production Performances from Original and Upscaling Systems (Tidal-Delta and Beach Composite System)

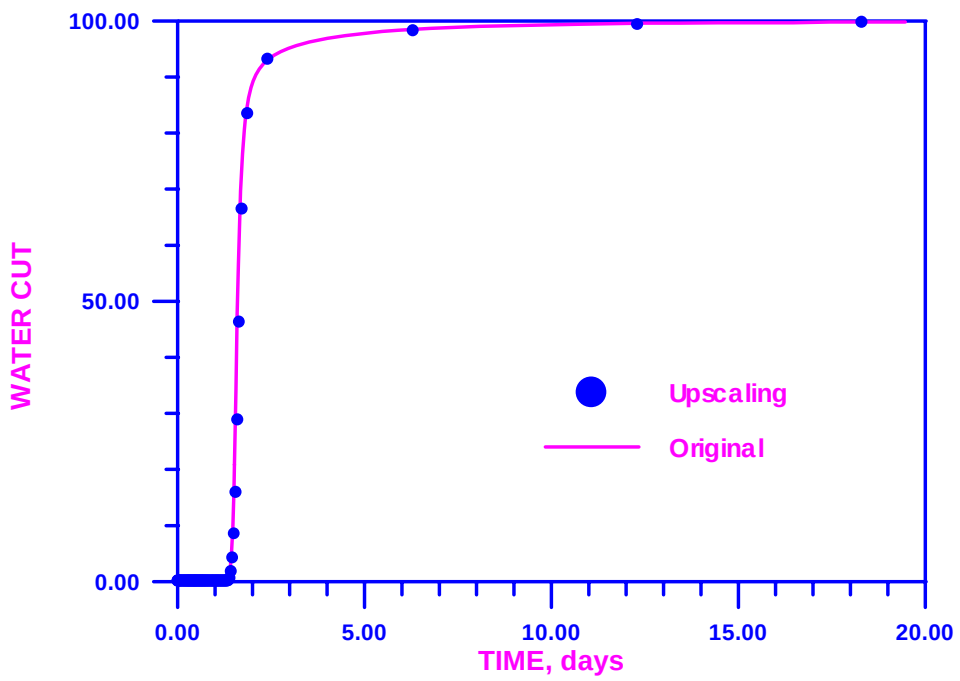


**Figure 4–22** Comparison of Water Cut at Production Wells from Original and Upscaling Systems (Tidal-Delta and Beach Composite System)

# 5.0 CONCLUSIONS

A primary purpose of this initial study is to investigate the applicability of wavelet analysis techniques to information transfer between different scales in petroleum reservoir rock property distributions, with a final goal being generation of realizations which incorporate all available information at different scales. A secondary purpose of this study is to use, for the first time, wavelet multiresolution analysis to scale up rock-fluid properties under multiple lithologies or facies and multiphase flow conditions. The ultimate goal is to determine an optimal grid system which can reasonably well capture the main characters of the original fine-scale system with known uncertainties. Based on our preliminary results discussed within previous sections of this report, the following conclusions can be stated:

1. We have presented a new scale-up method based on wavelet analysis for upscaling rock properties and rock-fluid properties. Compared to existing scale-up methods, implementation of this new method is easier, and computation is more efficient.
2. Excellent decomposition and reconstruction results of absolute permeability fields provide a promising basis for future work on generating realizations by incorporating all available information on different scales.
3. The new method falls in the category of the "effective properties method" (Chu et al. 1995a). By incorporating driving force information and complexity of geological structure into the new scale-up procedure, the degree of temporal, rate, and process dependencies is reduced.
4. Preliminary results demonstrate that the new upscaling method generates excellent equivalent properties for multiphase flow within a single facies and very reasonable upscaling interfacies properties in a multiple facies context.

# 6.0 NOMENCLATURE

$a$ = constant

$c$ = data sequence

$C_0$ = sill of semivariogram

$C_h$ = covariance matrix for hard data measurement errors

$C_M$ = covariance matrix

$C_{Mp}$ = a posteriori covariance matrix

$D_m$ = discrete approximation at scale $m$

$E_m$ = discrete detail signals at scale $m$

$f$ = water fractional flow

$G_h$ = matrix relating model hard data to model

$h(n)$ = coefficients (elements) for low-pass filter operator (matrix)

$H$ = low-pass filter operator or matrix

$g(n)$ = coefficients (elements) for high-pass filter operator (matrix)

$G$ = high-pass filter operator or matrix

$k$ = absolute permeability, md

$k_r$ = relative permeability

$n_j$ = relative permeability exponent of phase $j$

$n_{pc}$ = capillary pressure exponent

$N_{pc}$ = capillary number

$P_c$ = capillary pressure, $psi$

$P_m$ = projection on scaling subspace at scale $m$

$Q_m$ = projection on wavelet subspace at scale $m$

$S_j$ = saturation of phase $j$

$u$ = coordinate

$V$ = scaling subspace

$V_p$ = pore volume

$W$ = wavelet subspace

$x$ = coordinate

Greek:

| | | |
|---|---|---|
| $\alpha$ | = | weighting factor |
| $\delta$ | = | kroneclor delta function |
| $\gamma$ | = | semivariogram |
| $\lambda$ | = | scale parameters |
| $\mu$ | = | viscosity, cp |
| $\omega$ | = | frequency |
| $\phi$ | = | scaling function |
| $\sigma$ | = | standard deviation |
| $\psi$ | = | wavelet function |

Superscript:

| | | |
|---|---|---|
| -1 | = | inverse |
| - | = | equivalent, averaging or pseudo properties |
| T | = | transpose |

Subscript:

| | | |
|---|---|---|
| $1$ | = | aqueous phase |
| $2$ | = | oleic phase |
| $c$ | = | capillary-pressure related or capillary-pressure-dominated properties |
| $i$ | = | directional index |
| $j$ | = | directional index or phase index |
| $k$ | = | direction index |
| $L$ | = | spatial index |
| $m$ | = | level of scale or dimension of matrix |
| $n$ | = | spatial index or dimension of matrix |
| $r$ | = | relative properties |
| $v$ | = | viscous dominated |
| $w$ | = | water phase |
| $o$ | = | oil phase |

# 7.0 REFERENCES


Bacry, E., Mallat, S., and Papanicolaou, G. 1993. A Wavelet-Based Space-Time Adaptive Numerical for Partial Differential Equations. Internal report from New York University.

Brewer, K. E. and Wheatcraft, S. W. 1994. Including Multiscale Information in the Characterization of Hydraulic Conductivity Distributions. *Wavelet in Geophysics*. Foufoula-Georgiou and Kumar (eds.), Academic Press, Inc., p. 213–248.

Chang, M. M., Guo, G., Schatzinger, R., and Lawson, D. . 1994. Geological and Engineering Techniques for Prediction, Detection, and Evaluation of Reservoir Bounding Surfaces. DOE Topical Report NIPER/BDM-0053, 93 p.

Chu, L., Chang, M., and Lawson, D. 1995a. Review and Analysis of Upscaling Methods. NIPER/BDM-0158, July 1995.

Chu, L., Reynolds, A. C., and Oliver, D. S. 1995b. Reservoir Description from Static and Well-Test Data Using Efficient Gradient Methods. Paper SPE 29999, Proceedings of International Meeting on Petroleum Engineering, Nov. 14–17, 1995, Beijing, China, p. 467–482.

Daubechies, I. 1988. Orthonormal Bases of Compactly Supported Wavelets. *Comm. on Pure and Applied Math.* Vol. XLI, p. 901–996.

Daubechies, I. 1992. Ten Lectures on Wavelets. *SIAM.* Capital City Press.

Davis, A., Marshak, A., and Wiscombe, W. 1994. Wavelet-Based Multifractal Analysis of Non-stationary and/or Intermittent Geophysical Signals. *Wavelet in Geophysics.* Foufoula-Georgiou and Kumar (eds.), Academic Press, Inc., p. 249–299.

Grossmann, A. and Morlet, J. 1984. Decomposition of Hardy Functions into Square Integrable Wavelets of Constant Shapes. *SIAM J. Math. Analysis* 15(4), p. 723–736.

Kelkar, M. G. 1990. *Geostatistics.* Unpublished class textbook, p. 83–87.

Li, D, Cullick, A. S., and Lake, L. W. 1995. Scaled-Up of Reservoir Model Relative Permeability Using a Global Method. Paper SPE 29872 presented at 9th SPE Middle East Oil Show & Conference, Bahrain, March 11–14.

Mallat, S. 1989a. A Theory for Multiresolution Signal Decomposition: The Wavelet Representation. *IEEE Trans. on Pattern Anal. and Mach Intel.* 11(7), p. 674–693.

Mallat, S. 1989b. Multifrequency Channel Decompositions of Images and Wavelet Models. *IEEE Trans. on Acoustics, Speech and Signal Anal.* 37(12), p. 2091–2110.

Meyer, Y. 1993a. *Wavelets and Operators.* Cambridge University Press, New York, NY.

Meyer, Y., 1993b. *Wavelets: Algorithms and Applications.* SIAM, Philadelphia, PA.

Moridis, G. J., Nikolaou, M., and You, Y. 1995. The Use of Wavelet Transforms in the Solution of Two-Phase Flow Problems. Paper SPE 29144, proceedings of the 13th SPE Symposium on Reservoir Simulation, Feb. 12–15, 1995, San Antonio, TX, p. 521–530.

Morlet, J., Arens, G., Fourgeau, E., and Giars, D. 1982a. Wave Propagation and Sampling Theory—Part 1: Complex Signal and Scattering in Multilayered Media. *Geophysics* 47(2), p. 203–221.

Morlet, J., Arens, G., Fourgeau, E., and Giars, D. 1982b. Wave Propagation and Sampling Theory—Part 2: Sampling Theory and Complex Waves. *Geophysics* 47(2), p. 222–236.

Panda, M. N. 1994. A Forward Modeling of the Interwell Properties in Eolian Deposits. Ph.D. dissertation. University of Michigan.

Wickerhauser, M.V. 1993. *Adapted Wavelet Analysis from Theory to Software.* A. K. Peters, Ltd.

Wornell, G. W. and Oppenheim, A.V. 1992. Estimation of Fractal Geometry. *Water Resour. Res.* 24, p. 566–578.